Modeling the Failure Behavior of Countersunk Composite Bolted Joints Subjected to Monotonic Loading

By

Wendy Jean Paulson

Thesis

Submitted to the Faculty of the

Graduate School of Vanderbilt University

in partial fulfillment of the requirements

for the degree of

MASTER OF SCIENCE

in

Civil Engineering

May, 2017

Nashville, Tennessee

Approved:

Caglar Oskay, Ph.D.

Ravindra Duddu, Ph.D.

To my loving husband
and our ever-supportive families

ACKNOWLEDGEMENTS

This research could not have been performed without the gracious support and encouragement of many people. First and foremost, I would like to thank my research advisor, Dr. Caglar Oskay, for always seeing the potential in me and fostering my intellectual growth. Thank you for bringing me into your research group, for trusting me to take on the responsibilities of this project, for encouraging me to complete this thesis, and for supporting and guiding me throughout all of my research. I would also like to thank Dr. Ravindra Duddu for his advice and guidance, both on this thesis and throughout my graduate studies. My experience doing this research would not have been the same without the wonderful friendship of all of my labmates in the Multiscale Computational Mechanics Laboratory. Thank you all for the times you gave me advice, affirmed my work, and took the time to have an afternoon chat with me. Thanks to Xiang Zhang in particular for all of the times you stopped what you were doing to help me setup or fix my computer software so I could complete this work.

I would also like to thank Dr. Stephen Clay of the Air Force Research Laboratory for supervising this composites modeling work and providing support; your technical expertise and insightful questions have been invaluable in my research process. Thank you to Dr. Vipul Ranatunga of the Air Force Research Laboratory and Jonathan Bartley-Cho of Northrop Grumman Corporation for giving Vanderbilt the opportunity to be a part of Project 2, providing us with a host of experimental data, a chance to improve our composites model, and the support to be able to study these fascinating bolted joint setups. I gratefully acknowledge the financial support provided by the Aerospace Systems Directorate of the Air Force Research Laboratory and the Aerospace Systems department of Northrop Grumman Corporation as part of contract number FA8650-16-C-7614. I am also thankful for the fruitful, thought-provoking discussions that occurred as part of this project with Dr. Jim Lua and the other researchers at Global Engineering & Materials, Inc., and with Dr. Anthony Waas and his team of researchers at the University of Washington; thank you for the experience and knowledge you have so graciously and generously shared with us.

I truly appreciate the opportunity to be a part of the amazing work being done here in the Civil & Environmental Engineering department at Vanderbilt and for the chance to benefit from the incredible wealth of knowledge possessed by the faculty, staff, and students. I want to specifically thank Dr. Curtis Byers for encouraging me in my structural engineering aspirations

and for empowering me with powerful, relevant design instruction. I would also like to extend my gratitude to the Civil & Environmental Engineering department for their generous financial support which allowed me to pursue this endeavor.

I owe a debt of gratitude to my parents who have made sacrifices to open doors for me in my education and have been my cheerleaders in a way that no one else could have. Thank you to my incredible husband for your suggestion of applying to Vanderbilt and for your steadfast, kind support. Finally, thank you to all of the others who have come alongside me to show interest in my work; you have been a source of joy and encouragement and have made this such an incredible experience. I am so blessed by you all.

TABLE OF CONTENTS

Page

TABLE OF TABLES

Table Page

TABLE OF FIGURES

Figure Page

CHAPTER 1

INTRODUCTION

1.1 Motivation

Fiber reinforced polymer composite materials are highly attractive for use in aerospace vehicles due to their high strength to weight ratio, durability under fatigue loading, and ability to be easily customized. In order to use composite materials in actual structures, designers must be able to anticipate the structural response in various situations, representing different loading conditions. To ensure safe structures, there must be understanding of when and how failure could occur and reasonable expectations for the life cycle of each structural component. Currently, composite design and certification is performed predominantly based on physical experimentation. Not only is this approach costly, but it is also inefficient with regard to both time and materials. Because of the complexity of these materials, different configurations of the same material may exhibit dramatically different behavior. As such, a hierarchy of coupon to component testing is required for certification, as depicted in Figure 1. Moreover, material properties may vary from one production batch to the next due to differences in the curing cycles; thus, multiple experiments must be performed for each test configuration to avoid the effects of material variability.

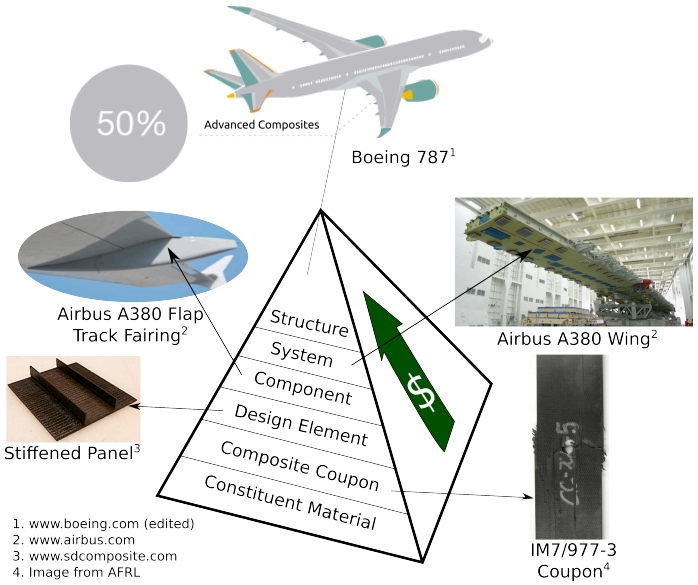

Figure 1. Testing hierarchy required for design certification of composite materials (courtesy of Michael Bogdanor)

All of these shortcomings point to the potential benefits of including computational failure modeling and prediction capability in design and certification, such that composite materials may be used to their full potential in aerospace vehicles. Computational models could be used to simulate a component under a variety of loading conditions, from which a critical case could be identified for experimental testing. The computational models also have the advantage of being able to build in the effect of material variability while directly representing the composite characteristics that could vary between components. If a reliable computational model could predict damage accumulation and failure in complex, realistic structural and loading scenarios, it could significantly reduce cost and lead time of composite structure implementation.

Model prediction of damage in composite materials is difficult due to the complexity of the failure mechanisms. Laminated fiber-reinforced polymer composites may fail due to matrix cracking, delamination between the plies of a laminated specimen, fiber failure, fiber kinking, or by interaction of these failure modes. Additionally, composite materials used in an aerospace vehicle's structure are typically mechanically attached by bolted joints to the other structural elements made of composite or metallic materials. Bolted joints present complications and mechanisms that are not yet well understood, such as bearing failure or failure under bearing-bypass. Bearing failure is a non-catastrophic failure mode which occurs progressively as a result of the concentrated compression forces between the bolt and composite laminate. The damage process begins with localized delamination between the outer plies, followed by matrix cracks, further intraply delamination, and fiber microbuckling, culminating in through-thickness shear cracks that cause failure [1]. While shear cracking remains the prominent failure mechanism for bearing, introducing an initial clamping force may suppress their formation, increasing bearing strength [2]. It has been shown that factors such as the specimen's lateral constraints and ply orientation also have significant influence on its bearing strength [3]. In multi-bolt joint configurations, the specimen may be subjected to bearing and the loads that bypass the hole through the surrounding composite material (i.e., bearing-bypass). In bearing-bypass, the failure mechanism depends on the portion of the load that is applied in bearing [4].

In order to reliably predict how these advanced materials behave in aerospace structures, a multiscale reduced order computational model, called the Eigendeformation-based Homogenization Method (EHM) has been developed by Oskay and coworkers [5, 6, 7]. The multiscaling approach is based on the computational homogenization theory [8]. EHM computes

the effective stress-strain behavior of the composite by numerically evaluating the constitutive response of a microscale representative volume element (RVE) or unit cell at each macroscopic material point, then spatially averaging the microscale response to describe the macroscale composite constitutive behavior. While many similar approaches are computationally cost prohibitive, EHM saves significant cost by computing some microstructural information prior to the macroscale analysis of the system. The key feature of the proposed modeling approach is that nucleation and propagation of damage within the composite are tracked at the microstructure, and no macroscale phenomenological failure criterion is used. EHM has been validated under pure composite specimen tests in compression and tension under both static [9, 10] and fatigue loading [11, 12, 13], and in complex load configuration scenarios, including impact [14], compression-after-impact [15, 16], and blast [17].

1.2 Air Force Research Laboratory CALE Project 2

Because most of the composite structures used in Air Force aircraft are built up using composite-to-composite and composite-to-metal joints, the Air Force Research Laboratory (AFRL) began a research program entitled "Composite Airframe Life Extension (CALE) Tools for Assessing the Durability and Damage Tolerance of Fastened Composite Joints" to study and develop tools to assess the remaining life and strength of these mechanical joints. This project, called CALE Project 2, aims to develop analysis capabilities to reliably predict failure of composite bolted joints under service loading from which structural integrity managers can assure continuing airworthiness. These same tools could then be extended for performing the analyses associated with composite structure design, allowing designers to more accurately meet design requirements without the additional cost and weight incurred by an overly conservative design. Significant work has been performed on damage failure analysis of open hole composite specimens under cyclic loading, and AFRL intends to assess through this program whether those same methods can be applied when the hole is filled by a fastener.

This research effort includes development of a progressive damage analysis (PDA) model for detailed damage analysis of specific features of aircraft structures involving bolted composite joints such that margins of safety may be identified or that residual strength may be maintained above design requirements. The model should predict damage initiation and damage growth to failure under fatigue loads applied to single or multi-bolt joint configurations. Multiscale

methods are well poised for this PDA prediction, as the interaction of local failure mechanisms on the microscale constituent level dictates the stress redistributions throughout cyclic loading.

In order to advance and verify the PDA model, extensive physical coupon-level specimen experimentation is included under this program. These tests will be performed on multiple configurations under both static and fatigue loading to adequately characterize the material behavior for PDA development. All PDA predictions will be performed blindly, followed by comparison with and recalibration to the experimental data obtained.

The Vanderbilt Multiscale Computational Mechanics Laboratory (MCML) was chosen as a PDA developer as part of CALE Project 2, to demonstrate and enhance the predictive capability of the EHM approach. This thesis work closely aligns with the project goals and program tasks performed under the timeline of Project 2, focusing on the computational modeling for monotonic loading prediction. All experiments referenced herein, unless otherwise noted, were performed under the direction and funding of this program.

1.3 Thesis Goals and Objectives

The goal of this thesis is to advance the state of the art in composite bolted joint computational modeling by the following objectives:

1. advance the modeling methods for prediction of composite bolted joints, as in meshing, contact formulation, and bolt material behavior,
2. assess the current capability of the PDA model in capturing the complex failure mechanisms and damage propagation behavior, and
3. make improvements to the model to better predict the behavior of multiple configurations of composite bolted joints under a range of monotonic tests.

1.4 Thesis Structure

This thesis is organized as follows. In Chapter 2, the multiscale modeling approach that underlies the composite material behavior is briefly introduced with its main governing equations. The material definition and the modeling implementation schemes generally followed in building and meshing the models for simulation are addressed in Chapter 3. Chapter 4 details some preliminary work on the simulation of two configurations of composite-metallic joints, providing conclusions which serve as the basis of the direction of further development. These

improvements are then addressed in Chapter 5 through a more rigorous prediction scheme. Chapter 6 summarizes the main conclusions from this work as it stands and suggests future work that would complement these studies.

CHAPTER 2

EIGENDEFORMATION-BASED HOMOGENIZATION METHOD

EHM is a multiscale computational homogenization-based approach, used in composite specimens to model their mechanical response and predict their material failure. The response of the macroscopic structure is solved not by an explicit constitutive relation, but instead by spatially averaging, or homogenizing, the numerically evaluated response of a microscale RVE or unit cell at each macroscopic material point of the composite. Damage is considered in the constituent materials at the microstructural level, which then coalesces to cause macroscopic failure, and as such, no phenomenological failure criterion is required for the composite structure. To reduce computational cost of evaluating a full microstructure model, the approach evaluates the unit cell problem by employing a reduced approximation basis to homogenize or localize the stress and strain fields between the multiple spatial scales. The microscale displacement field is defined using influence functions, which express the microstructural variations with numerical Green's functions that can be computed prior to macroscale analysis, as they depend solely on the RVE geometry and elastic properties. Additionally, a coarse discretization of the microstructure, associated with the distinct microstructural parts, is employed to approximate the inelastic strain field (or eigenstrains). The details of this method are given in [5, 6].

A particular EHM model was developed with the microstructure of a specific laminated, unidirectional carbon fiber reinforced polymer called IM7/977-3 in conjunction with a previous AFRL program [10, 13]. IM7/977-3 is idealized as a 60% fiber-volume fraction square packed unit cell made up of four parts, corresponding to the fiber and matrix constituent materials, separated by the four different dominant failure mechanisms: one part fiber in the center, subject to fracture, one part matrix, subject to transverse matrix cracking, a second matrix part, subject to delamination, and a final matrix part, subject to a combination of both matrix failure mechanisms. The unit cell is shown in Figure 2.

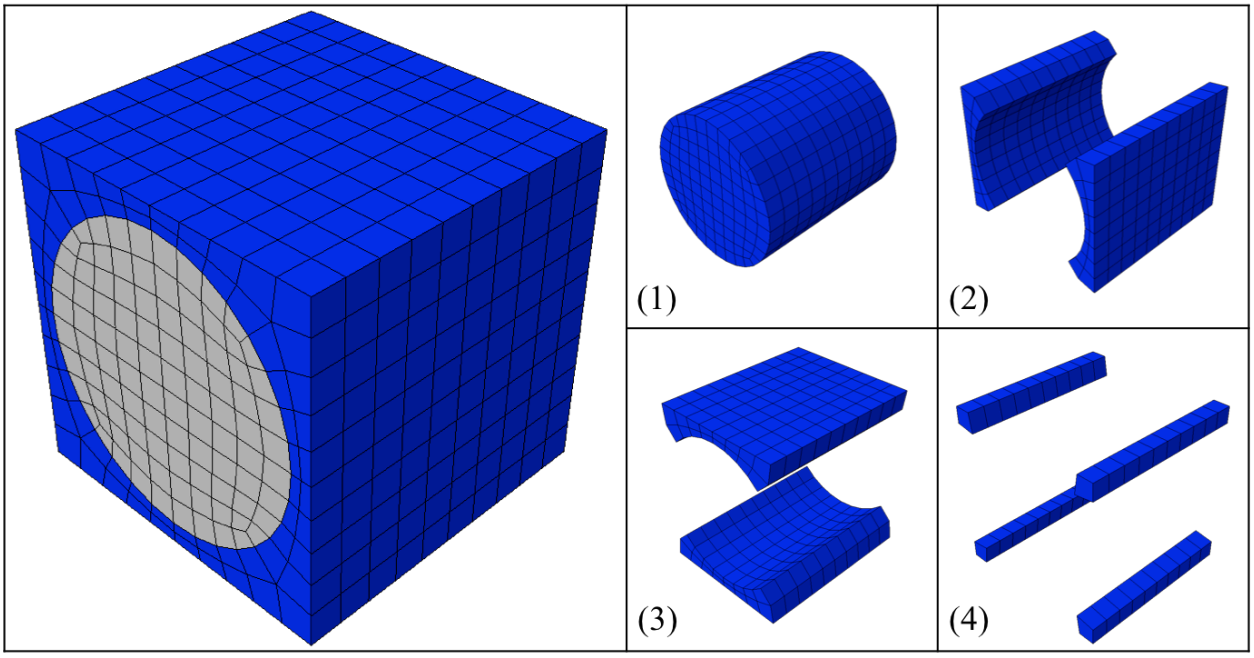

Figure 2. Unit cell used in this research with the 4-part Eigendeformation-based Homogenization Method model

The macroscale problem defined over the specimen domain, $\mathbf{\Omega}$, is represented by the macroscopic equilibrium equation, kinematic equation, and the boundary conditions, respectively, as follows in Equations 1-4:

$$\nabla \cdot \bar{\boldsymbol{\sigma}}(\mathbf{x},t) + \bar{\mathbf{b}}(\mathbf{x}) = 0; \;\; \mathbf{x} \in \mathbf{\Omega}; \;\; t \in [0, t_0] \tag{1}$$

$$\bar{\boldsymbol{\epsilon}}(\mathbf{x},t) = \nabla^s \bar{\mathbf{u}}(\mathbf{x},t) \tag{2}$$

$$\bar{\mathbf{u}} = \hat{\mathbf{u}}(\mathbf{x},t); \;\; \mathbf{x} \in \mathbf{\Gamma}_u \tag{3}$$

$$\bar{\boldsymbol{\sigma}} \cdot \mathbf{n} = \hat{\mathbf{t}}(\mathbf{x},t); \;\; \mathbf{x} \in \mathbf{\Gamma}_t \tag{4}$$

where $\bar{\boldsymbol{\sigma}}$ is the homogenized macroscale stress field, $\bar{\mathbf{b}}$ is the body force, $\mathbf{x}$ and t describe the spatial and temporal positions, $\bar{\boldsymbol{\epsilon}}$ is the homogenized strain, $\bar{\mathbf{u}}$ is the macroscale displacement, and $\hat{\mathbf{u}}$ and $\hat{\mathbf{t}}$ represent the boundary displacements and tractions, respectively [10].

The domain of the microstructure is subdivided into two or more materially uniform parts that comprise the reduced order model (ROM) of the microstructure, where γ indicates the part number and n is the total number of parts. The homogenized macroscale stress field is calculated based on the boundary value problem given by:

$$\bar{\boldsymbol{\sigma}} = \sum_{\Delta=1}^{n} \left[1 - \omega^{(\Delta)}\right] \left[\bar{\mathbf{L}}^{(\Delta)} : \bar{\boldsymbol{\epsilon}} + \sum_{\alpha=1}^{n} \bar{\mathbf{P}}^{(\alpha\Delta)} : \boldsymbol{\mu}^{(\alpha)}\right] \tag{5}$$

solved over the domain of the microstructure. The part inelastic strains, $\boldsymbol{\mu}^{(\gamma)}$, which are the unknowns of the reduced order microscale boundary value problem, are computed as the solution to the system of equations given by

$$\sum_{\Delta=1}^{n} \left\{ \left[1 - \omega^{(\Delta)}\right] \left[\hat{\mathbf{A}}^{(\alpha\Delta)} : \bar{\boldsymbol{\epsilon}} + \sum_{\gamma=1}^{n} \hat{\mathbf{B}}^{(\alpha\Delta\gamma)} : \boldsymbol{\mu}^{(\gamma)}\right] \right\} = 0 \quad \forall \alpha = 1, 2, \ldots, n \tag{6}$$

In these equations $\bar{\mathbf{L}}$, $\bar{\mathbf{P}}$, $\hat{\mathbf{A}}$, and $\hat{\mathbf{B}}$ are the precomputed coefficient tensors derived using the influence functions [5, 6].

2.1 Constitutive Model for Composite Constituents

The damage evolution within each of the four parts of the EHM model is driven by the damage equivalent strain for the part, $\upsilon^{(\gamma)}$, as defined by

$$\upsilon^{(\gamma)} = \sqrt{\frac{1}{2}(\boldsymbol{F}^{(\gamma)}\hat{\boldsymbol{\varepsilon}}^{(\gamma)}) : \hat{\mathbf{L}}^{(\gamma)} : (\boldsymbol{F}^{(\gamma)}\hat{\boldsymbol{\varepsilon}}^{(\gamma)})} \tag{7}$$

where $\hat{\varepsilon}^{(\gamma)}$ is composed of the part principal strains, calculated as the eigenvalues of the part strain $\boldsymbol{\epsilon}^{(\gamma)}$, $\hat{\mathbf{L}}^{(\gamma)}$ is the rotated elastic moduli tensor for the part with respect to the principle strains, and $\boldsymbol{F}^{(\gamma)}$ is the strain weighting matrix to account for material anisotropy between tension and compression. The strain weighting matrix is defined by

$$F^{(\gamma)} = \begin{bmatrix} h_1 & 0 & 0 \\ 0 & h_2 & 0 \\ 0 & 0 & h_3 \end{bmatrix} \qquad h_\xi = \begin{cases} 1 \text{ if } \hat{\epsilon}_\xi > 0 \\ c^{(\gamma)} \text{ otherwise} \end{cases} \quad \text{for } \xi = 1, 2, 3 \tag{8}$$

in which $c^{(\gamma)}$ is the tension/compression anisotropy material parameter for the part.

The damage potential is found as a function of the damage equivalent strain in the part by the arctangent evolution function:

$$\Phi(\upsilon^{(\gamma)}) = \frac{\arctan(a^{(\gamma)}\langle \upsilon^{(\gamma)} - \upsilon_0^{(\gamma)} \rangle - b^{(\gamma)}) + \arctan(b^{(\gamma)})}{\frac{\pi}{2} + \arctan(b^{(\gamma)})} \tag{9}$$

where $a^{(\gamma)}$, $b^{(\gamma)}$, and $\upsilon_0^{(\gamma)}$ are material parameters that control the damage evolution function's shape. The material parameter $b^{(\gamma)}$, which accounts for the discrepancy in evolution between shear and normal loading conditions, is defined as

$$b^{(\gamma)} = k_b b_s^{(\gamma)} + (1 - k_b) b_n^{(\gamma)} \tag{10}$$

$$k_b = \frac{\gamma_{max}^{(\gamma)}}{\gamma_{max}^{(\gamma)}/2 + \epsilon_{max}^{(\gamma)}}; \ \in [0, 1] \tag{11}$$

where $b_s^{(\gamma)}$ and $b_n^{(\gamma)}$ are the parameters controlling shear and normal loading respectively and k_b is calculated by Equation 11. $\gamma_{max}^{(\gamma)}$ is the maximum engineering shear strain experienced in the part, and $\epsilon_{max}^{(\gamma)}$ is the maximum absolute principal strain [10, 18, 19].

Finally, damage, $\omega^{(\gamma)}$, is defined as the damage potential evaluated at the maximum damage equivalent strain over the loading history, given by the following equations [10].

$$\omega^{(\gamma)} = \Phi(\upsilon_{\max}^{(\gamma)}) \tag{12}$$

$$\upsilon_{\max}^{(\gamma)} = \max_{0 \le \tau \le t} \{\upsilon^{(\gamma)}(\tau)\} \tag{13}$$

2.2 EHM Implementation Strategy

The computational algorithm employed to perform an EHM analysis of a composite specimen is shown in Figure 3. An in-house code is utilized to conduct the microstructure preprocessing, including the EHM model construction, ROM part generation, and coefficient tensor calculation. The resulting coefficient tensors are input to the macroscale finite element model.

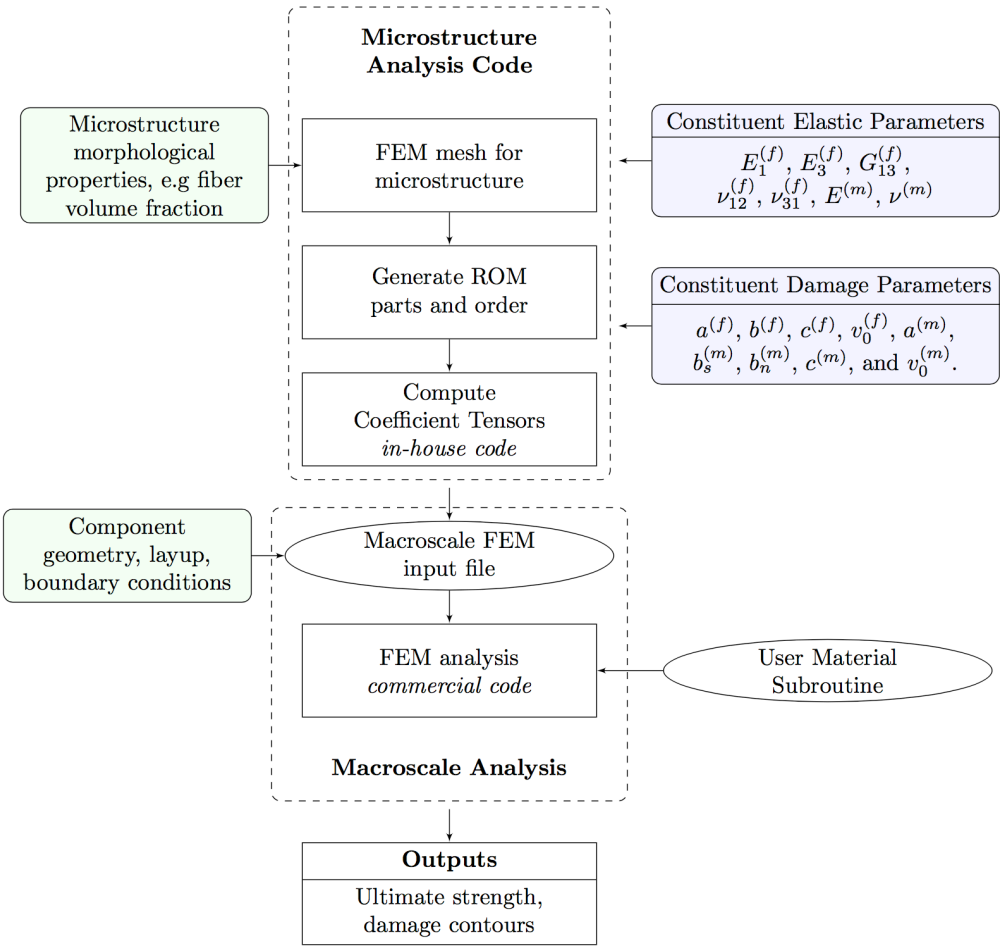

Figure 3. Computational flowchart for Eigendeformation-based Homogenization Method composite specimen analysis, adopted from [20]

All modeling is performed with commercial finite element analysis software, Abaqus. Each quadrature point on the macroscale is represented by a microstructure, over which the boundary value problem is solved numerically for equilibrium and damage evolution. This microscale information is then passed to the macroscale problem. A user material subroutine (UMAT) performs this routine; given the macroscopic strain increment and internal state variables, it localizes the strain to each part of the ROM, evolves damage in each part, checks for microscale equilibrium, computes the macroscopic stress and tangent stiffness matrix, and passes Abaqus the necessary information to continue analysis [10].

CHAPTER 3

NUMERICAL SPECIMEN AND MATERIAL DEFINITION

3.1 Numerical Specimen

The macroscale specimens investigated in this study are carbon fiber reinforced polymer (CFRP) laminated composites, where each ply of the laminate is a layer of polymer material impregnated with unidirectional fibers. The specimens are defined by their layup, or the fiber direction in each of the plies layered together to create the full specimen. The fiber direction is defined by the convention displayed in Figure 4.

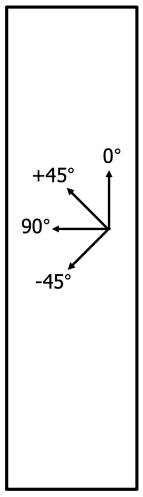

Figure 4. Specimen fiber direction standard nomenclature on a generic specimen geometry

The CFRP numerical specimen was generated according to specific experimental test geometries in Abaqus following a standard in-house procedure, as was developed by Bogdanor [20]. Each ply present in the specimen layup was modeled separately, assigned an orientation, and meshed such that the mesh aligned with the fiber direction, due to prior testing that showed this useful for the most accurate damage pattern prediction. Once each ply was created, they were assembled to create the layup specimen.

In the assembly process, the plies were added in the order specified by the layup definition and placed on top of each other. Then, the plies were connected by adding tie constraints between them. Node-to-surface type tie constraints were used in order to be able to

apply the boundary conditions appropriately. Node-to-surface type ties connect slave nodes to the nearest master node(s), which ensures that even with nonconforming meshes between the master and slave surfaces, the edges of the specimen act as one piece. Boundary conditions were applied to the specimen to mimic test experiment conditions. Care was taken to simplify the assemblies as much as possible to reduce computational cost without changing the resulting behavior.

Experimental cases including bolts considered a step prior to the loading step in which preload force on the bolt was exerted using the built-in Abaqus bolt preloading capability. The bolt preload was defined as a force value consistent with the experiments discussed in what follows. Abaqus applies the bolt preload by shrinking or stretching the bolt such that the correct force is observed. It is common in experiments for the bolt preload to relax during the loading stage; therefore, in the numerical model, the length of the bolt was fixed immediately after preload, such that the preload force was not held constant throughout the loading but allowed to appropriately relax.

3.2 Material Definition

This study focuses on IM7/977-3 composite specimens in the [44/44/11] family where 44% of the plies are either +45 or -45 degree plies, 44% are 0 degree plies, and the remaining plies are 90 degree plies. Common ranges for overall IM7/977-3 composite level elastic properties are shown in Table 1, in comparison to the actual property values simulated by this EHM model. The material constituent elastic parameters and damage parameters used as input properties for the EHM analyses, which were calibrated prior to this study [10], are reported in Table 2 and Table 3.

Table 1. Experimental range of composite elastic material properties compared to model simulated properties

Elastic Property	Description	Experimental Range	EHM Model Simulated Value
V_f	Fiber volume fraction	0.60-0.65	0.60
E_{11t} [Msi]	Longitudinal elastic modulus in tension	22.86-23.83	22.6
E_{11c} [Msi]	Longitudinal elastic modulus in compression	18.91-19.93	18.9
E_{22} [Msi]	Transverse elastic modulus	1.28-1.30	1.28
v_{21}	Longitudinal Poisson's ratio	0.0175	0.0175
v_{12}	Transverse Poisson's ratio	0.320	0.3197
G_{13} [Msi]	Shear modulus	0.716-0.757	0.716

Table 2. Calibrated constituent material elastic parameters [10]

Elastic Property	Description	Fiber Material Value	Matrix Material Value
E_1 [Msi]	Transverse elastic modulus	1.81	0.54
E_{3t} [Msi]	Longitudinal elastic modulus in tension	37.33	0.54
E_{3c} [Msi]	Longitudinal elastic modulus in compression	31.26	0.54
G_{13} [Msi]	Shear modulus	21.18	-
v_{21}	Transverse Poisson's ratio	0.291	0.37
v_{31}	Longitudinal Poisson's ratio	0.206	0.37

Table 3. Calibrated constituent material damage parameters and descriptions [10]

Property	Description	Value
$a^{(f)}$	Governs magnitude of fiber failure	0.050562
$b^{(f)}$	Governs ductility of fiber failure	273.66
$c^{(f)}$	Controls compression/tension anisotropy of fiber	1.4481
$v_0^{(f)}$	Threshold value below which no damage occurs in fiber	1367
$a^{(m)}$	Governs magnitude of matrix failure	0.001592
$b_n^{(m)}$, $b_s^{(m)}$	Governs ductility of matrix failure	15, -3.2
$c^{(m)}$	Controls compression/tension anisotropy of matrix	0.535
$v_0^{(m)}$	Threshold value below which no damage occurs in matrix	636.2

CHAPTER 4

PRELIMINARY BLIND PREDICTION STUDY

Two geometric configurations, referred to from herein as SLEP-C and IRAD, were studied in order to assess the current capability of EHM in the prediction of the behavior of composite bolted joints. From this portion of the study, areas of improvement were identified for a more in-depth study discussed in Chapter 5.

4.1 Geometry Preparation

The SLEP-C specimen was a protruding head bolted joint specimen, and the IRAD specimen was a countersunk bolted joint specimen. Each experimental configuration used the specimen with the dimensions given in Figure 5, and were made of a $[45/-45/0_2/45/-45/0/90/0/45/-45/0_2/45/-45/0_2/90]_S$ layup.

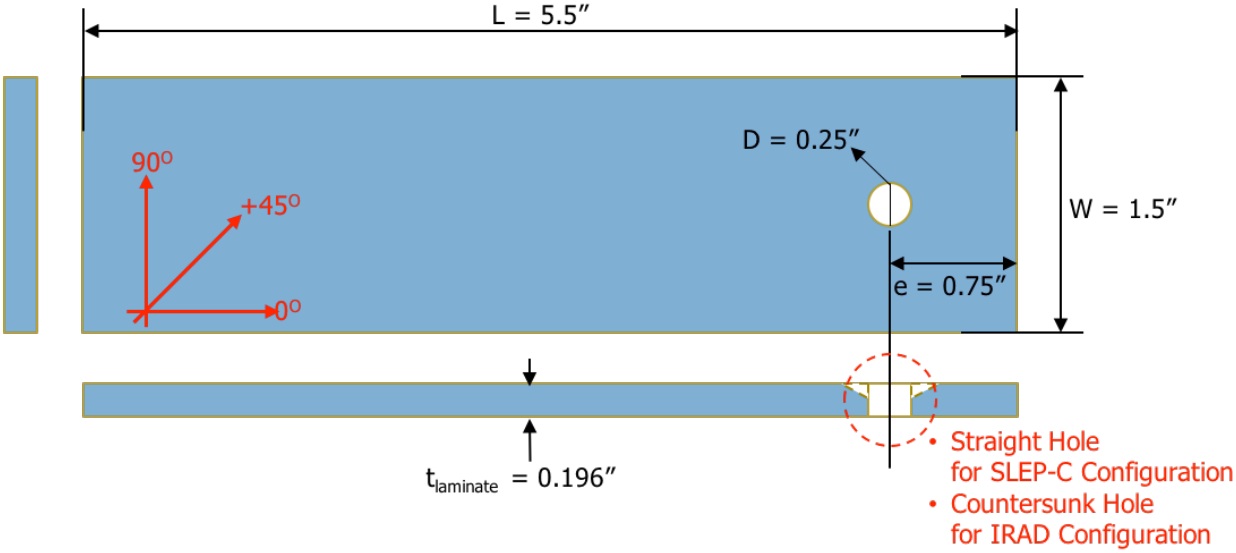

Figure 5. Composite specimen definition for SLEP-C and IRAD experiments (figure used courtesy of Jonathan Bartley-Cho of Northrop Grumman Corporation)

The assemblies were simplified in both cases to remove unnecessary computational cost, such that the IRAD configuration was modeled from grip to grip and the SLEP-C configuration was modeled from the edge of the tab on the specimen to the free end of the specimen. Experimental

setup dimensions are given in Figure 6 and Figure 7. The bolts were ¼" diameter 13-8 stainless steel and the remaining fixture parts were modeled as 17-4 stainless steel.

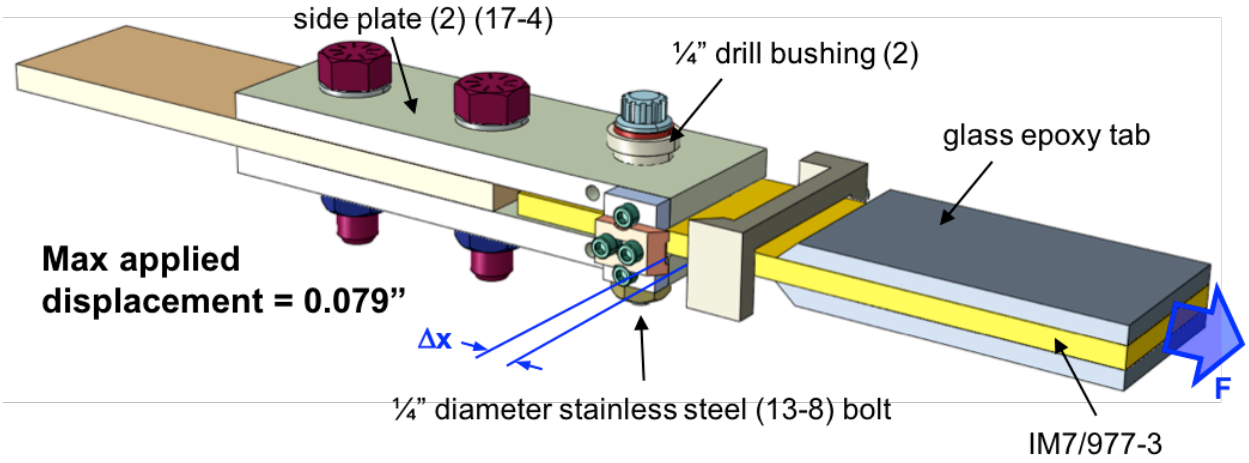

Figure 6. SLEP-C experimental test setup diagram (figure used courtesy of Jonathan Bartley-Cho of Northrop Grumman Corporation)

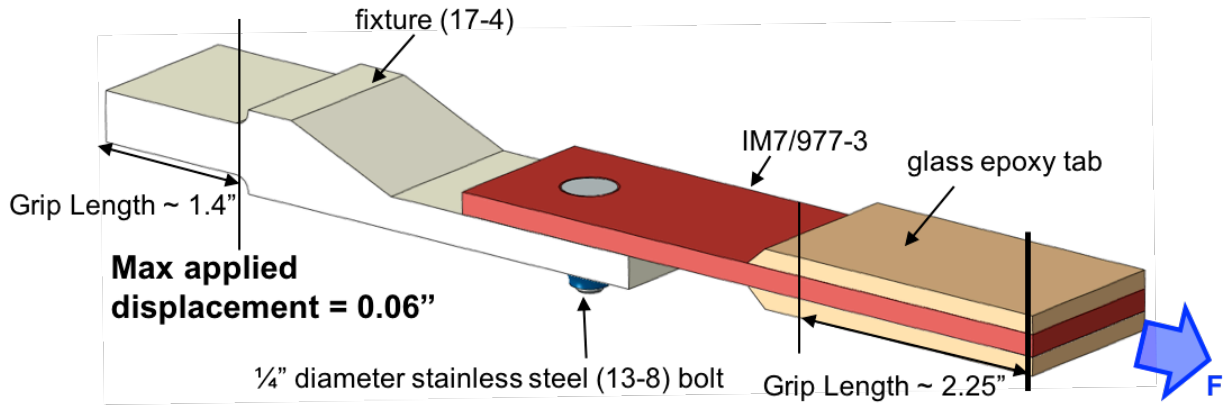

Figure 7. IRAD experimental test setup diagram (figure used courtesy of Jonathan Bartley-Cho of Northrop Grumman Corporation)

The specimen meshing scheme and model assemblies are depicted in Figure 8, where the modeled portions of the fixture are colored blue and the modeled portions of the specimen are gray. In order to be able to approximately capture the effect of elongation, the mesh size was chosen to be about 0.01 inches in length closest to the hole, radially increasing within a square inch area of refinement to 0.04 inches and to 0.75 inches throughout the rest of the specimen. The mesh was aligned with the direction of the fiber within the area of refinement. Each

configuration used a specimen built from 36 plies, each with 0.005 inch thickness. The SLEP-C specimen consisted of 117,820 solid brick elements, and the IRAD specimen had 128,894.

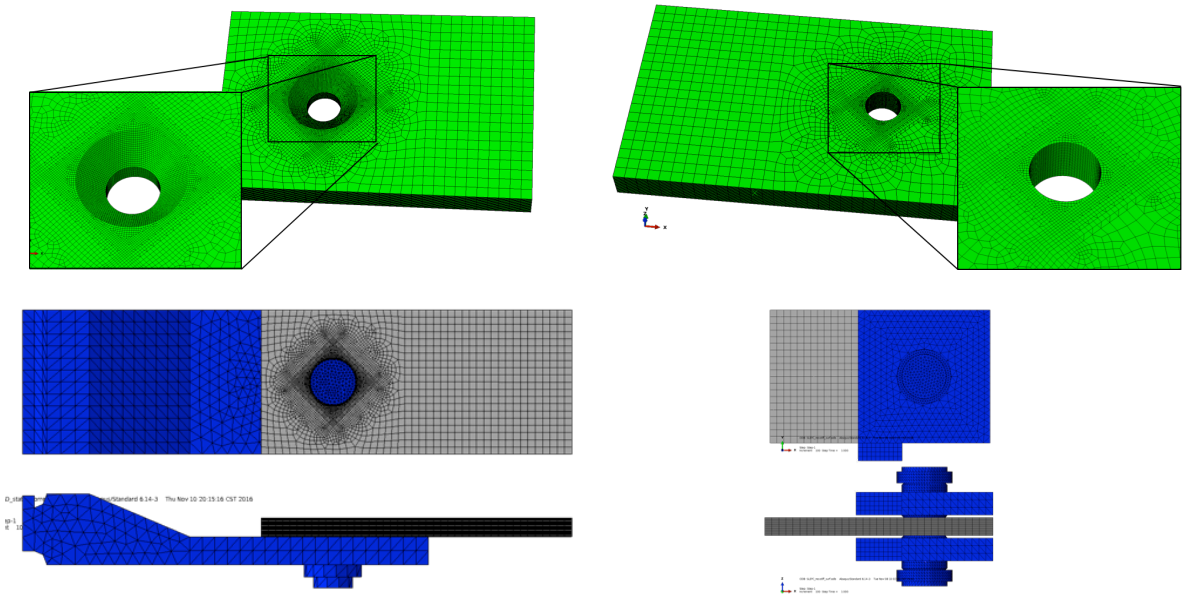

Figure 8. (Left) IRAD and (Right) SLEP-C meshes with refinement zones around bolt hole and assemblies

In general, the separate pieces of the fixture were held together with tie constraints, and hard contact was enforced between the specimen and any portion of the fixture to which it could come in contact. Contact in the IRAD case also included friction in the tangential direction with a friction coefficient of 0.45. The preload force on the bolt was exerted using the internal Abaqus capability to a given nominal force of 400 pounds. For both configurations, load was applied as a monotonically increasing displacement of 0.06 and 0.079 inches, respectively, applied at the edge of tab for the SLEP-C case and at the edge of grip for the IRAD case. For SLEP-C, the top and bottom side plates were pinned in all three directions on the right edge shown in Figure 8, and for IRAD, the top and bottom edges where the fixture was gripped were constrained in all three directions.

4.2 Model Development for Bearing

Bearing behavior introduces the mechanism of localized damage on the contact surface between the bolt and specimen, and there are two extremes for what could occur once the initial contact surface is fully damaged. Either the debris of that damaged region could fall out immediately upon full damage, or the debris could remain and continue to transfer force to the

next layers of specimen. Depending on the test setup, any given bearing situation could closely mimic one of these two scenarios, or fall somewhere in between.

Immediate removal of debris could be modeled as a situation where elements are deleted and contact evolves as the damage states evolve. Using this method, once an element reaches a defined level of damage, the UMAT instructs Abaqus to remove the element from the mesh. At this point, the bolt must find contact with the next layer of material in the deleted element's place. The difficulty with using this method within the implicit version of Abaqus (Abaqus\Standard) comes in defining the contact at the beginning between surfaces which are not yet touching, but could potentially touch at some point during the simulation. In order to accomplish this, Abaqus requires the use of the general contact formulation, in which Abaqus automatically determines the contact surfaces and applies contact on those surfaces. This formulation allows surfaces which may be on the interior at a given point in the simulation to be on-the-fly defined as in contact once they reach the exterior. While possible, this approach leads to convergence difficulties as contact is lost and reestablished between the bolt and the specimen following element deletion. Furthermore, between the time when full contact is lost due to element deletion and when the contact is regained with the next row of elements, the force carrying capability of the specimen drops significantly, causing pronounced force fluctuations. Such fluctuations were not observed in the experiments.

In the idea of load transfer through debris, as the countersunk bolt is being driven into the specimen in compression, the bolt begins to overturn, trapping the debris between it and the straight portion of the bolt hole. On the opposite side with the straight portion of the bolt hole, the hole is blocked by the nut, which also keeps the debris from falling out. In the blind predictions, this idea is employed.

The proposed method for modeling this phenomenon is through the residual stiffness idea. This method can be visualized in Figure 9.

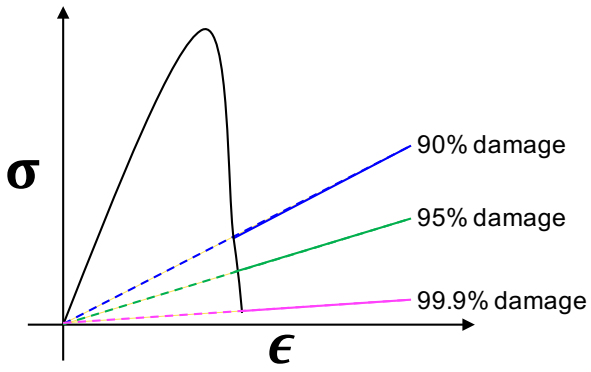

Figure 9. Residual stiffness idea

At the point on the stress strain curve at which the damage in one of the ROM parts reaches a given percentage, a residual stiffness is imparted to the material in that part at the slope with which it could connect to the curve's origin. The higher the damage percentage threshold, the more significant the stiffness value. All of the damage percentages investigated in this study are high enough that the residual stiffness is significantly less than the original stiffness of the material. It is important to note that the composite response is sensitive to the amplitude of residual stiffness, as is demonstrated by the SLEP-C configuration simulated with residual stiffness governed by damage thresholds ranging from 90-95% of full damage, shown in Figure 10. The residual stiffness must therefore be calibrated based on experiments.

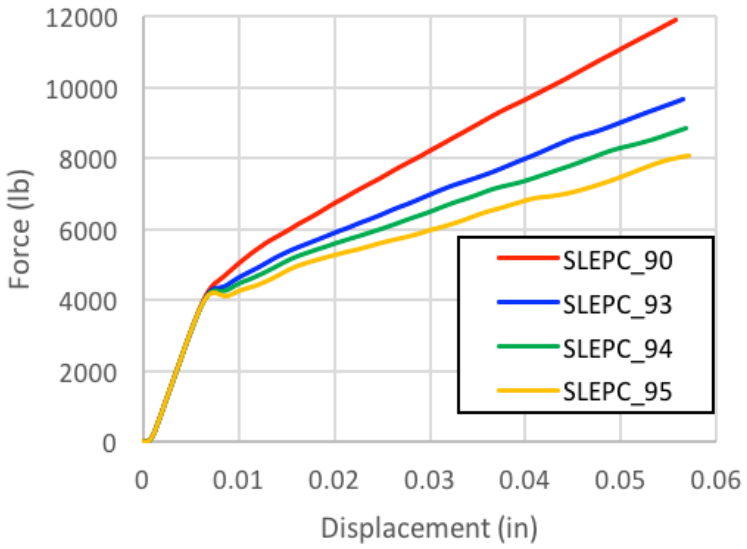

Figure 10. Initial parametric study of the effect of various residual stiffness damage threshold percentages

In the blind predictions, the residual stiffness was set to 94% damage threshold (or 6% of the initial stiffness). The chosen value corresponds to the smallest residual stiffness that allowed full execution of the simulations without encountering numerical convergence issues.

4.3 Blind Predictions

Force displacement curves were extracted from the simulation results, where force was calculated as the total reaction force on the cross section at the end of the specimen and displacement was calculated for SLEP-C from a virtual extensometer, labeled as Δx in Figure 6, and for IRAD by the overall displacement of the specimen. The curves are given in Figure 11 and Figure 12.

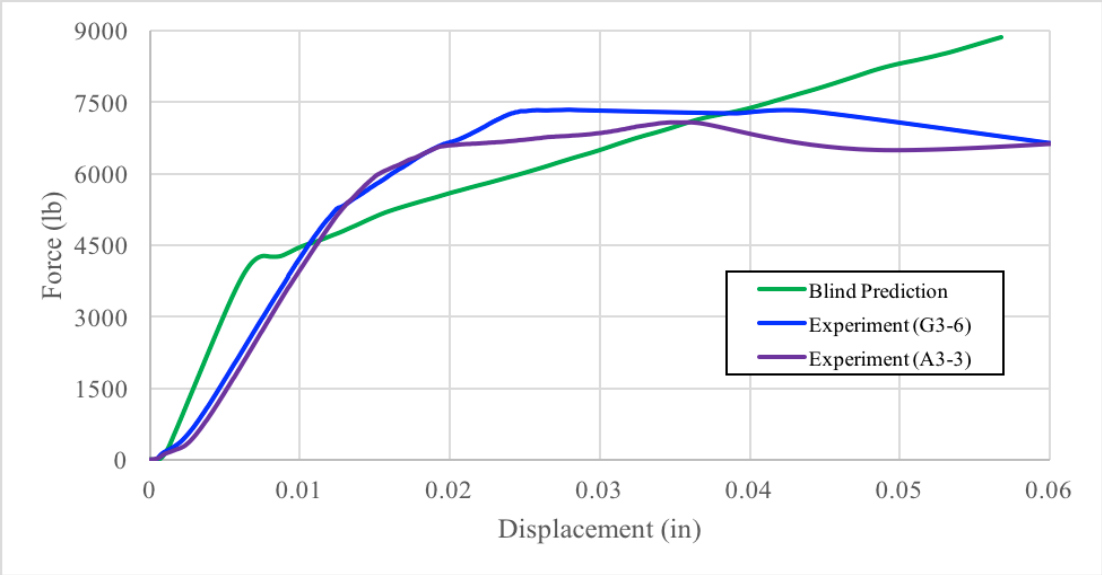

Figure 11. SLEP-C displacement controlled blind predictions compared with experimental results

The SLEP-C configuration had a reasonable overall match with the experiments. The stiffness predicted by the simulations for both the SLEP-C and IRAD configurations is significantly higher than the experimentally observed stiffness. The post-peak behavior predicted by the model shows a finite and constant slope after the onset of initial failure observed near the hole. The experimental data demonstrate a flat force-displacement curve.

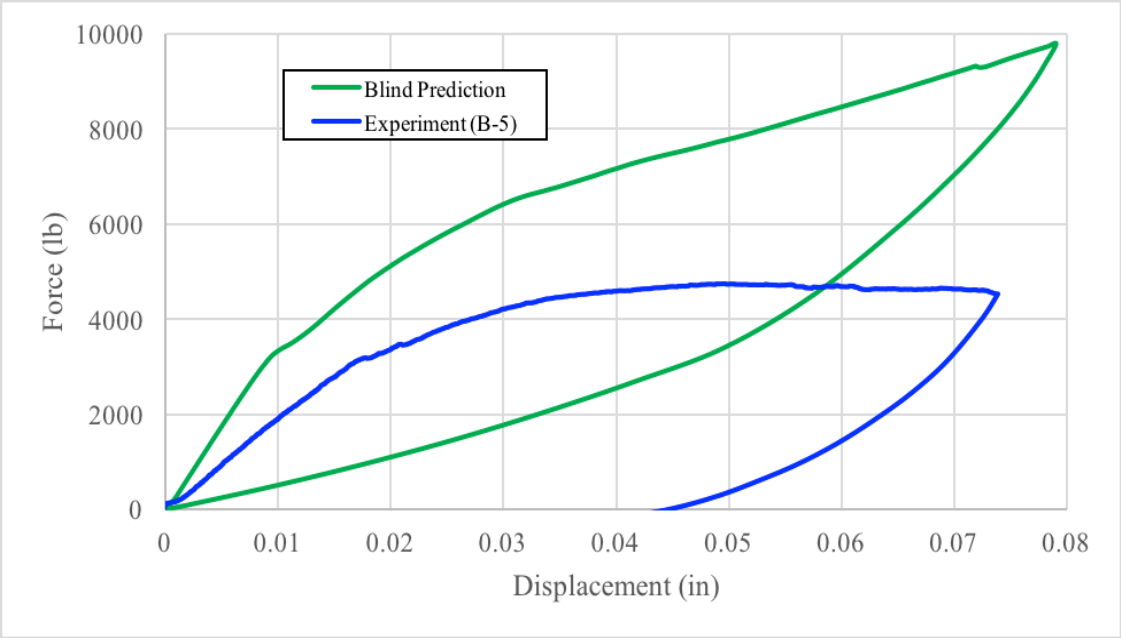

Figure 12. IRAD blind predictions compared with experimental results

Damage was tracked throughout the simulation, where the final damage state predicted by the PDA model is shown in Figure 13 and Figure 14 as compared to the experimental specimen pictures, shown here specifically for the matrix material. The red portions of the specimen have reached full damage, the blue portions of the curve are yet pristine, and a gradient color between the two states has accumulated some, but not complete, damage.

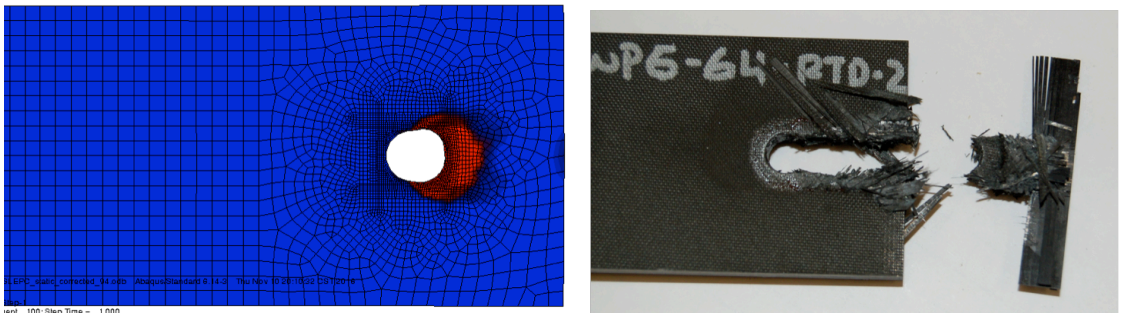

Figure 13. SLEP-C qualitative damage state comparison between experiment at 0.25" extensometer displacement and simulation at 0.06" extensometer displacement

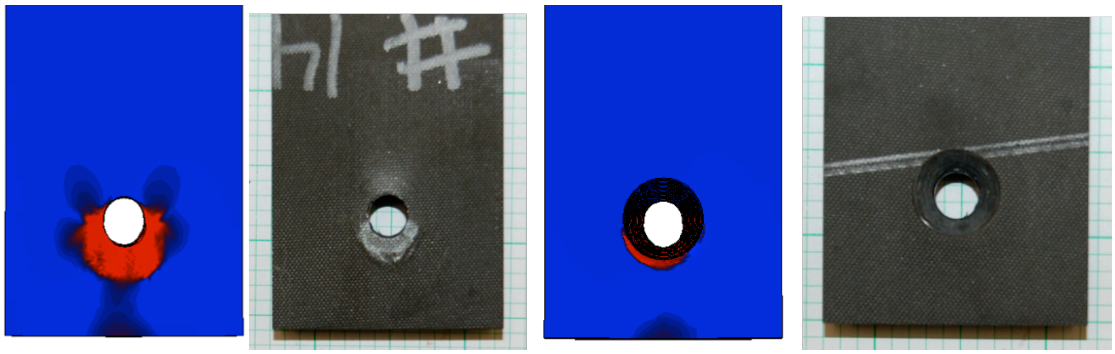

Figure 14. IRAD qualitative damage state comparison between experiment and simulation at 0.079" overall displacement

It should be noted that in the SLEP-C experiment damage plot, a full shear out behavior of the bolt is observed, but that this occurred at a later point of damage than the PDA model was tasked to predict. The IRAD damage prediction shows good agreement with the experimental results.

4.4 Recalibration Studies

Numerical investigation and parametric analyses were performed to better understand the root cause of the discrepancies between the predicted and observed behavior in the SLEP-C and IRAD configurations, which are discussed below.

4.4.1 Addressing Stiffness

The stiffness of the experiments and model predictions for the SLEP-C and IRAD specimens were significantly mismatched, because of what was later determined to be the assumption that the bolt and the fixture act together, and as such, could be represented as one piece. This assumption is revisited in testing described in Section 5.4.1.1.2 and will be discussed in more detail there.

4.4.2 Addressing Post-peak Behavior

Using residual stiffness of 6% of initial stiffness over predicts the post failure stress, as observed in the post-peak shape of the experimental force displacement curves. Simulations were performed using lower residual stiffness. The SLEP-C simulation results using residual stiffnesses between 94 and 99% damage threshold are shown in Figure 15, from which it was determined that even though the 99% prediction provides the most stable residual stiffness, it

does not provide enough strength as compared to the experiments, and all other damage thresholds, similar to 94%, have too much residual stiffness.

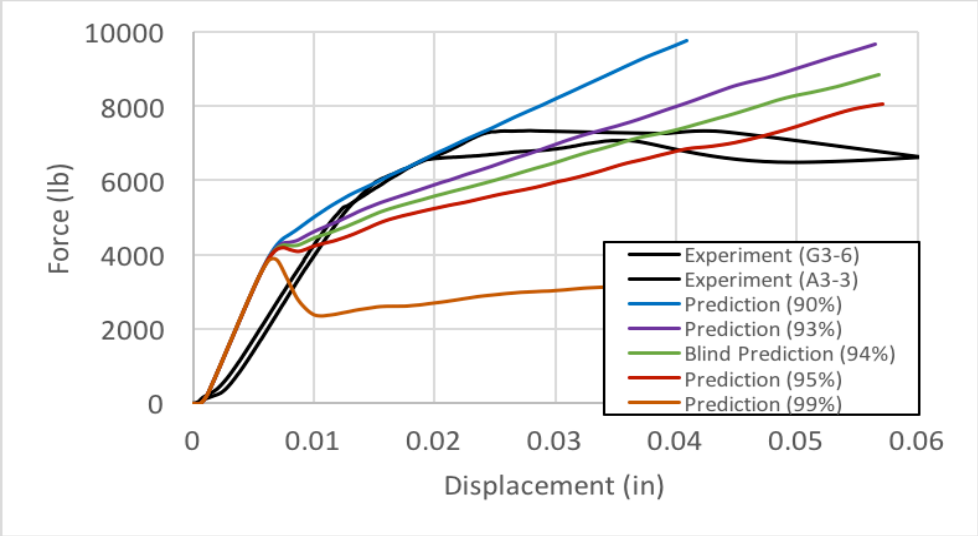

Figure 15. Comparison of SLEP-C experimental post-peak behavior to residual stiffness simulations with damage thresholds between 94 and 99%

Upon closer examination of the SLEP-C experimental results, it was discovered that the test had been performed under load control, rather than the modeled displacement control. A couple simulations were performed under the load control condition, the results of which are presented in Figure 16.

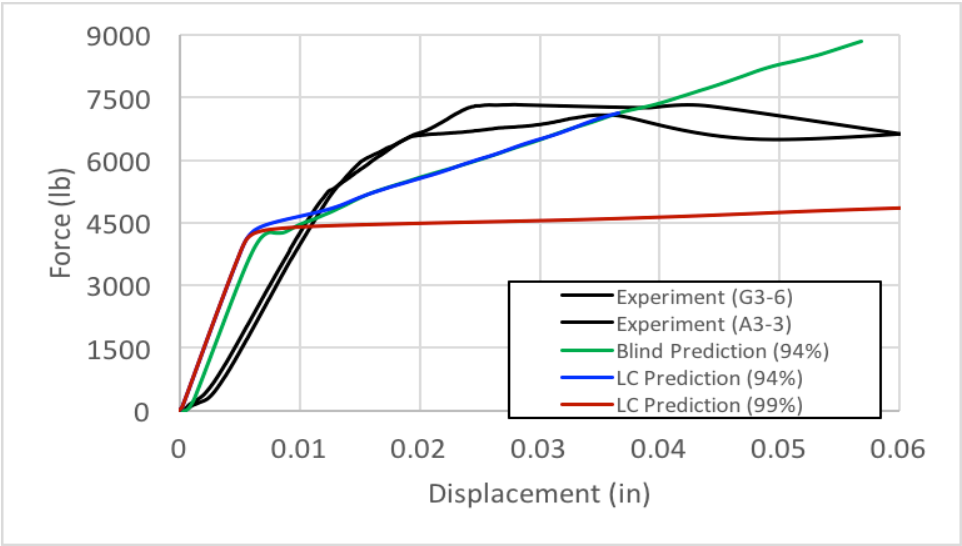

Figure 16. SLEP-C simulations performed using load control as in experiments, rather than displacement control

From the load control tests, we still do not see very accurate post-peak behavior, but the peaking effect of using 99% as the residual stiffness damage threshold seen in Figure 15 is smoothed, showing closer agreement with the experiments.

It is well understood that unregularized continuum damage models are mesh dependent and that the size of the mesh may have an effect on the damage evolution. The material parameters were calibrated using a larger mesh size than that with which this project models the specimen; thus, the SLEP-C prediction was run using a mesh very similar to that used in parameter calibration. The results are shown in Figure 17.

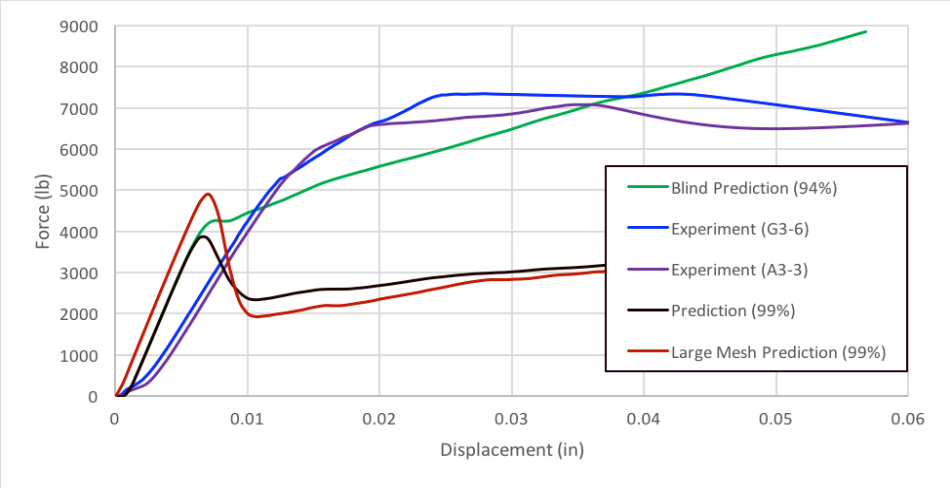

Figure 17. SLEP-C experimental post-peak behavior as compared with model prediction using calibration mesh and current mesh

From this, we see that the larger mesh did increase the ultimate strength, as expected, but the shape of the force displacement curve was not otherwise affected.

4.4.3 Addressing Unloading Behavior of IRAD specimen

The results of the IRAD experiment indicate that the bolt undergoes plastic deformation at the applied load magnitude. In the blind prediction, the bolt was modeled using an elastic material. In order to determine the effect of including bolt plasticity, a test case was run with Von Mises type plasticity attributed to the bolt, extracted from the material stress strain data.

The results are shown in Figure 18. From this, we see that at least a significant portion of the permanent deformation observed in the experimental results can be explained by the

behavior of the bolt, and that the bolt plays an important role in the overall behavior of the system.

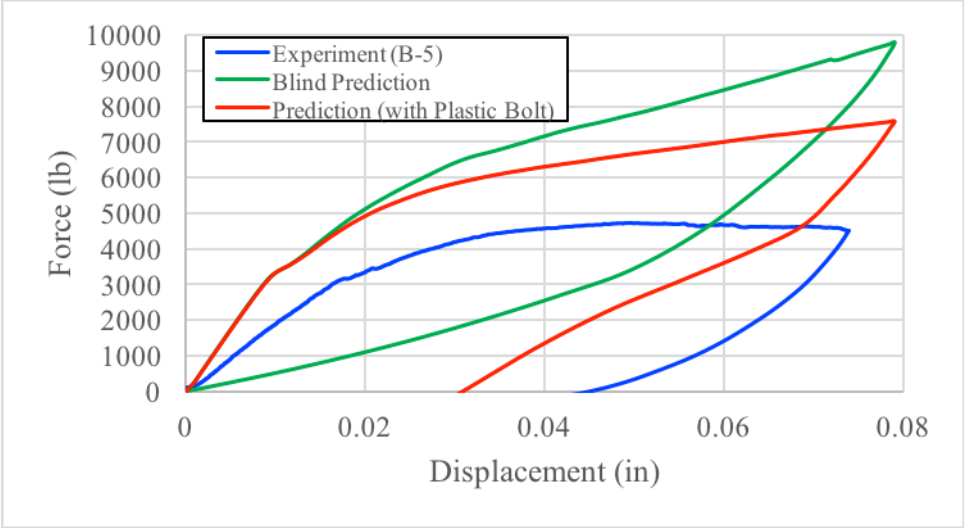

Figure 18. Comparison of original IRAD blind prediction with elastic bolt to prediction with plastic bolt

4.5 Identified Areas for Improvement

As a result of these preliminary predictions, some necessary improvements were identified for EHM to be able to reliably predict the performance of composite bolted joints. Because a significant (roughly 75%) error was observed in capturing the stiffness of both IRAD and SLEPC specimens between the model and the experiments, further studies testing stiffness are needed to ensure the correct stiffness capture for the composite specimens used in this study. As previously mentioned, these investigations are addressed in Section 5.4.1.1.2. Since fatigue loading is at relatively low load amplitudes, the effect of capturing the linear portion of the force-displacement curve is likely to be more critical than the static tests.

Additionally, to better capture the damage propagation, the residual stiffness method requires further investigation. A closer look at the fiber and matrix damage models should be performed, potentially leading to a recalibration of the form of the shear and compressive properties and/or models. This investigation is critical to capturing the details of the response when large amount of deformation is observed near the bolt hole. Some enhancement to the computational model or modeling methods may be required.

CHAPTER 5

IN-DEPTH BOLTED JOINT BLIND PREDICTION STUDY

The broad goal of this in-depth study is to incorporate the model improvements identified through the SLEP-C and IRAD predictions. In order to make the model improvements, a series of additional tests were employed, starting with a plain, open hole specimen, building to a filled hole and eventually a single lap bearing specimen. These three different general experimental setups considered composite specimens of the [44/44/11] family of IM7/977-3. The progression from a very simple test setup to a problem with a complex bearing-type situation will allow the model to be enhanced in a very controlled, logical manner, addressing first the material behavior for this production batch, next the effect of bolt presence and preload, and finally the full bearing behavior. To study the effect of specimen thickness, specimens were considered with three different ply counts (27 plies, 36 plies, and 45 plies) subjected to each of the experimental test setups. The laminate layup in each case was $[+45/0/-45/0/90/0/-45/0/+45]_x$, where x represents 3, 4, and 5 for the three configurations, respectively. A summary of the experiments performed by blind prediction is given by Table 4.

Table 4. Summary of experimental test setups

Geometry	Open Hole (OH)	Filled Hole (FH)	Single Shear Bearing (SSB)
Static Tension	27, 36 ply	27, 36 ply	27, 36, 45 ply
Static Compression	-	-	36 ply
Constant Amplitude Fatigue	-	27, 36 ply	27, 36, 45 ply
Block Spectrum Fatigue	-	27, 36 ply	27, 36, 45 ply

5.1 Geometry Preparation

The specimens in the different models were created using the same meshing scheme described in Section 4.1 and implemented on the specific geometries for each case. Each layup in these cases included 21 countersunk plies, and the remaining plies had straight holes, each ply

having 0.0053 inch thickness. The specimen element counts for each configuration are given in Table 5.

Table 5. Number of solid brick elements for each test setup

Configuration	Open Hole (OH)	Filled Hole (FH)	Single Shear Bearing (SSB)
1	123,166	123,166	119,448
2	159,950	159,950	149,292
3	-	-	189,315

The specimen dimensions for the Open Hole (OH) and Filled Hole (FH) tests are shown in Figure 19, where the OH test setup only considers the specimen and the FH test setup includes the countersunk bolt, aluminum backing plate, washer, and preloading nut. Three inch long aluminum tabs were also installed for the testing setup on the front and back of the specimen along the top and bottom, though not pictured.

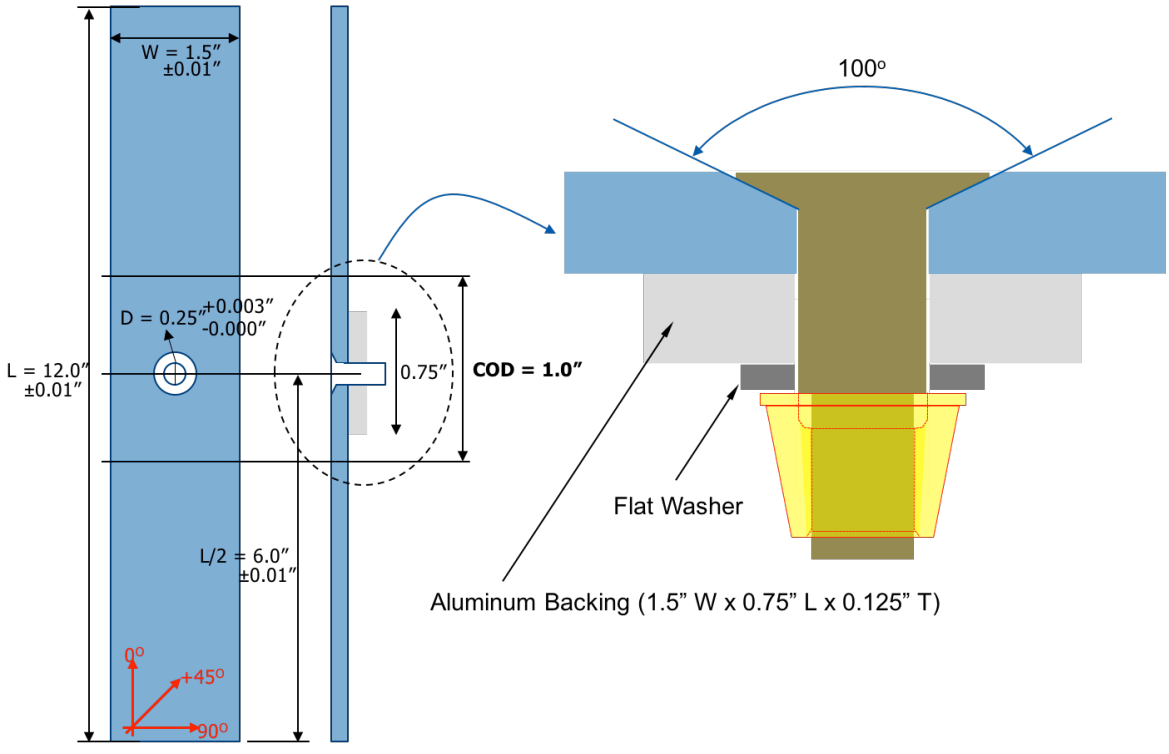

Figure 19. Experimental test setup and specimen dimensions for Open Hole and Filled Hole configurations (figure used courtesy of Jonathan Bartley-Cho of Northrop Grumman Corporation)

The OH and FH configurations used in the model are shown in Figure 20 and Figure 21. Both the OH and FH specimens were modeled from edge of grip to edge of grip and loaded by displacement control on one end; the grip length in both cases was about 2.25 inches. The opposite end was modeled as if it were gripped by the machine, such that the top and bottom edges were fixed in the non-loading directions, and the entire back face was fixed in the loading direction. In the FH experiment, the bolt was preloaded to 2350 pounds.

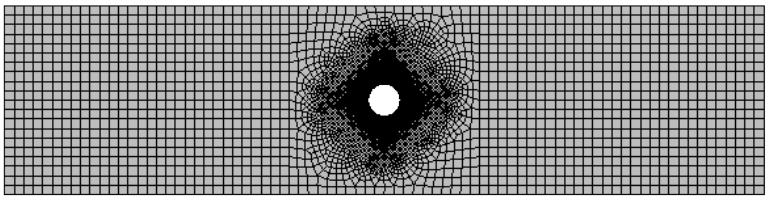

Figure 20. Open Hole configuration model (from top)

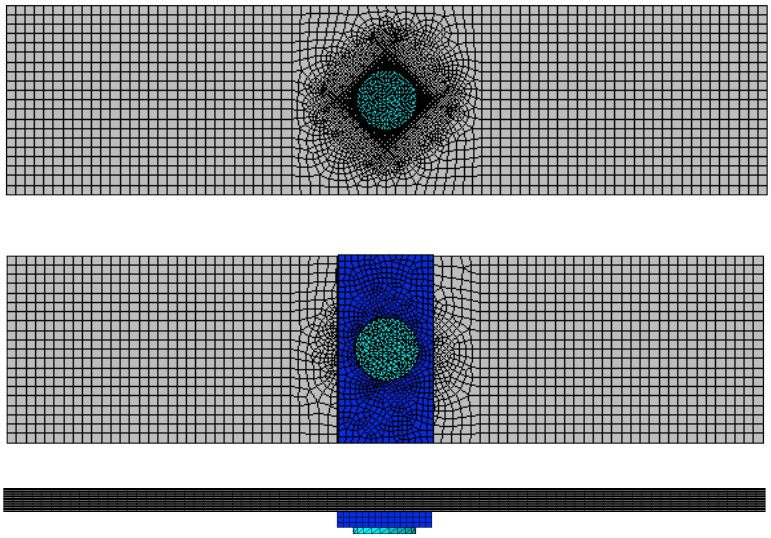

Figure 21. Filled Hole configuration model (from top, bottom, and side)

The Single Shear Bearing (SSB) experimental setup is defined in Figure 22. The dimensions for the upper and lower grip lengths vary based on the configuration, as given with the loading information in Table 6.

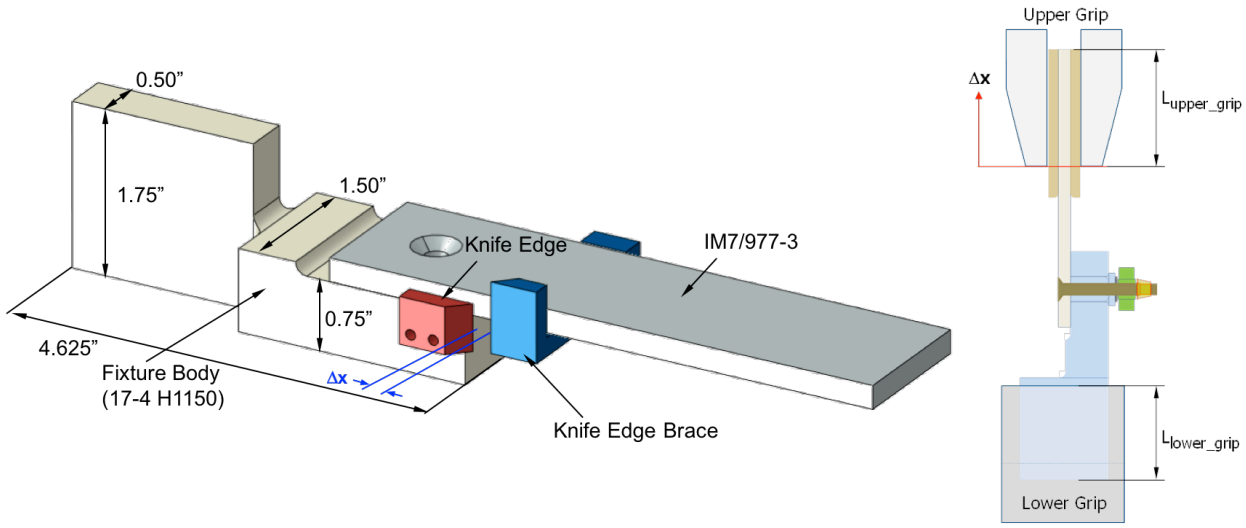

Figure 22. Experimental test setup and specimen dimensions for Single Shear Bearing configuration (figure used courtesy of Jonathan Bartley-Cho of Northrop Grumman Corporation)

Table 6. Additional Single Shear Bearing setup and testing dimensions

Laminate Configuration	**L_{upper_grip} [in]**	**L_{lower_grip} [in]**	**Δx_{max}= Maximum End Displacement [in]**
1	2.25	1.6	0.04
2	2.5	2.0	0.12
3	2.25	1.6	0.04

The specimen was loaded by displacement control. The back block of the fixture was gripped by the MTS machine and fixed in all three directions, while the face of the specimen was pulled in tension away from the fixture. This imparted a compressive force on the opposite side of the specimen hole. At first, the bolt and fixture were assumed to act as one congruent piece; however, this assumption was revisited through elastic test cases performed. As in the IRAD cases, any contact surfaces between the fixture (including the bolt) were modeled as hard contact with a 0.45 friction penalty coefficient, and where applicable, the bolt preload was applied at 2350 pounds. The SSB model configuration is shown in Figure 23.

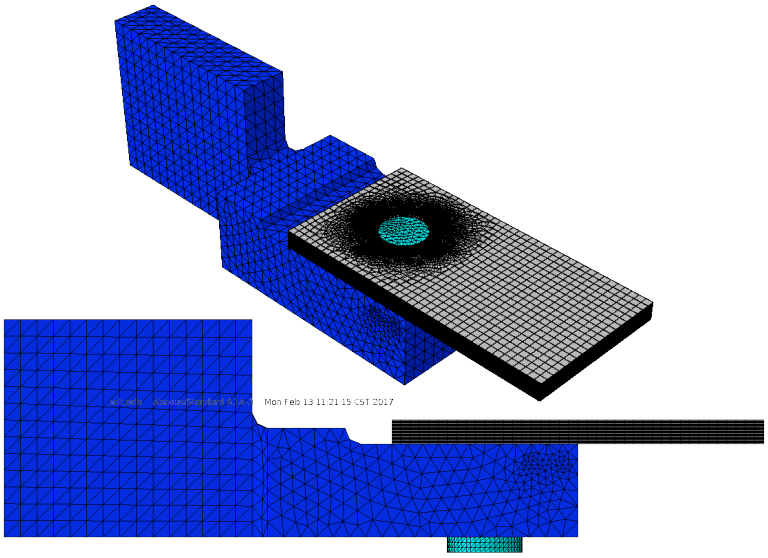

Figure 23. Single Shear Bearing configuration model (from overall and side)

5.2 Open Hole Model Static Predictions

The OH static tests were predicted in order to identify a baseline performance of the model in predicting the countersunk hole specimens. This work fed well into establishing the stiffness of the material and implementing changes if necessary.

5.2.1 Blind Predictions

Force displacement curves were extracted from the simulation results. Force was defined as the sum of reaction forces on the pulled face, and displacement was calculated by a virtual crack opening displacement (COD) gage held between two knife edge braces centered around the hole with an original distance of 1 inch, as depicted in Figure 19. The curves are shown in Figure 24, as compared with the experimental data curves.

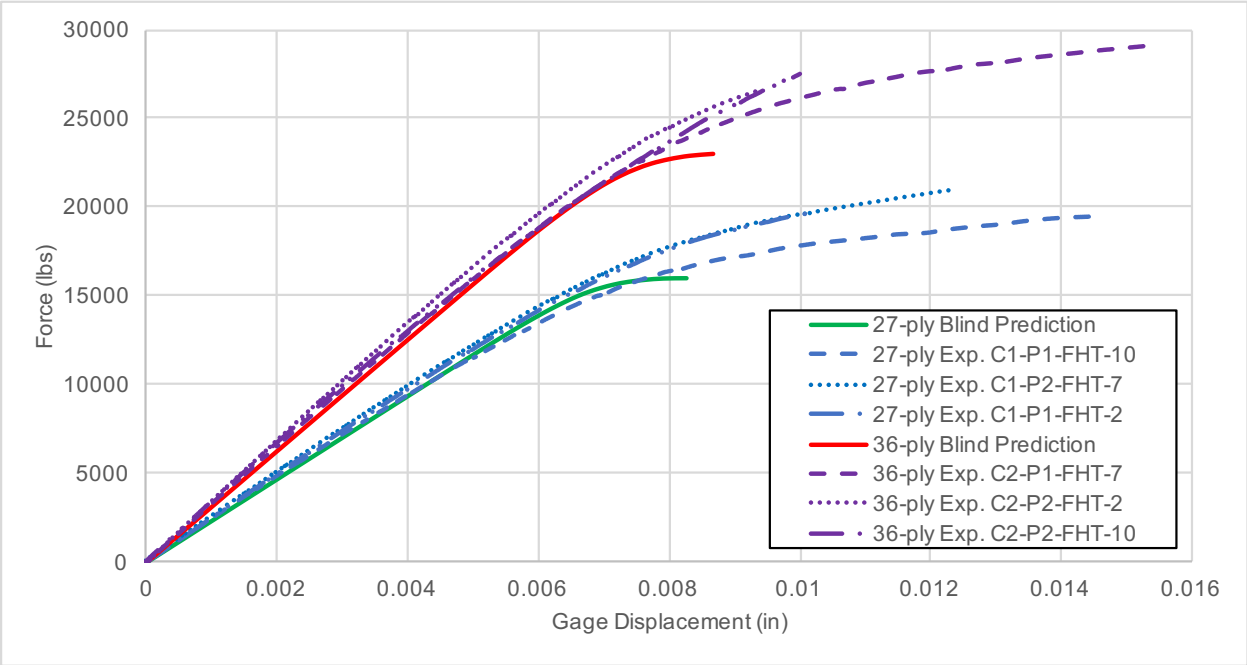

Figure 24. Static Open Hole tension P-d curve blind prediction

Both configurations show excellent stiffness match. The model predictions also show the ability to capture the nonlinear behavior observed in the experiments, but an under prediction of the strength.

The final predicted damage state (i.e., damage state at the peak of the P-d curve) of fiber damage, matrix damage, and delamination damage on the specimens are shown in Figure 25 for Configuration 1 and in Figure 26 for Configuration 2.

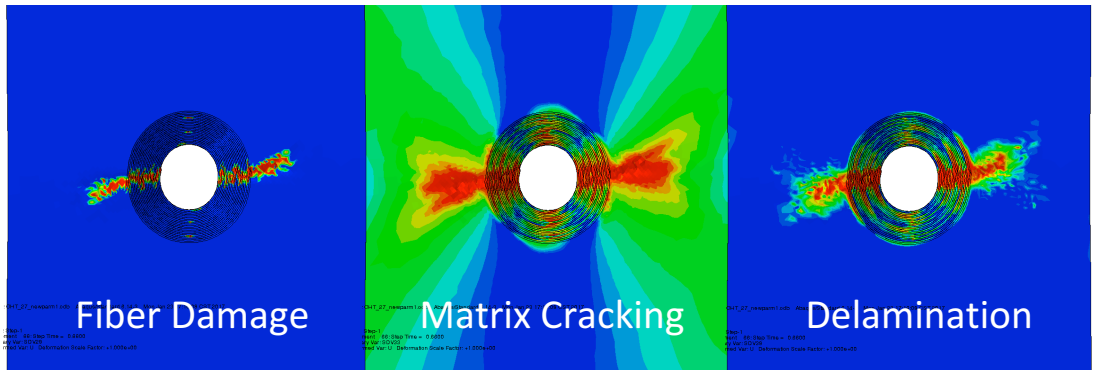

Figure 25. 27-ply (Configuration 1) Open Hole damage pattern predictions for fiber, matrix, and delamination damage

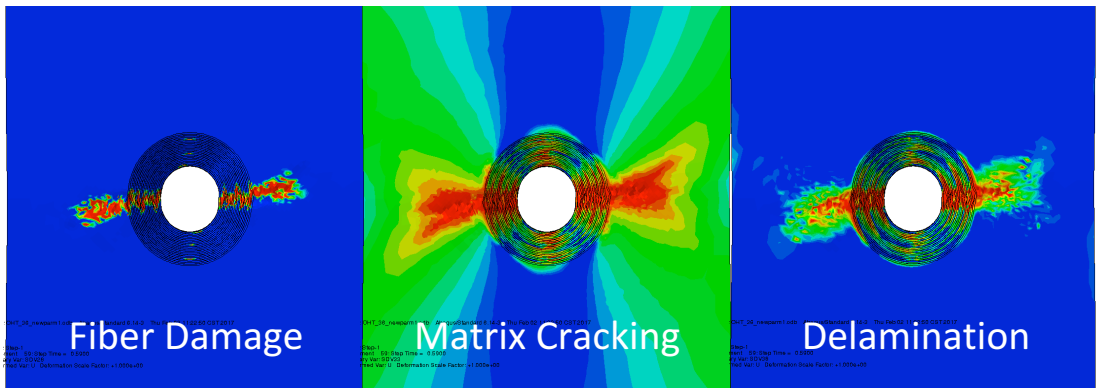

Figure 26. 36-ply (Configuration 2) Open Hole damage pattern predictions for fiber, matrix, and delamination damage

The damage plots can be qualitatively compared to the experimental pictures of the damaged specimens given in Figure 27, which are representative of the damage patterns seen in both configurations in all of the damaged specimens.

Figure 27. Open Hole experimental overall damage patterns for qualitative comparison

5.2.2 Recalibration

Model recalibration was performed in order to enhance the force-displacement performance of the model in the OH predictions. All damage model parameters used in the

blind prediction phases of this thesis project were calibrated from data generated by AFRL [10, 13]. The prior calibration assumed a mesh size of about 0.04 inches in element side length; whereas in this study, the mesh size varied from about 0.01 inches to 0.075 inches in element side length. It is well known that continuum damage models are mesh sensitive, and while a mesh insensitive damage model is under development, the current model used in this project is sensitive to mesh size. The effect of mesh size was shown for the SLEP-C configuration, addressed in Section 4.4.2. In order to overcome the effect of mesh size difference between the calibration simulations and this study's simulations, a parametric recalibration was performed to increase the fiber strength, changing its damage parameters, as given in Table 7.

Table 7. Material parameters from Open Hole blind prediction compared to recalibration

Property	**OH Blind Prediction**	**OH Recalibration**
$a^{(f)}$	0.050562	0.0025
$b^{(f)}$	273.66	18.0
$c^{(f)}$	1.4481	1.4481
$v_0^{(f)}$	1367	1367
$a^{(m)}$	0.001592	0.001592
$b_n^{(m)}$, $b_s^{(m)}$	15, -3.2	15, -3.2
$c^{(m)}$	0.535	0.535
$v_0^{(m)}$	636.2	636.2

The recalibrated results compared with experimental data and the blind predictions are shown in Figure 28, displaying good agreement both in stiffness and in ultimate strength prediction.

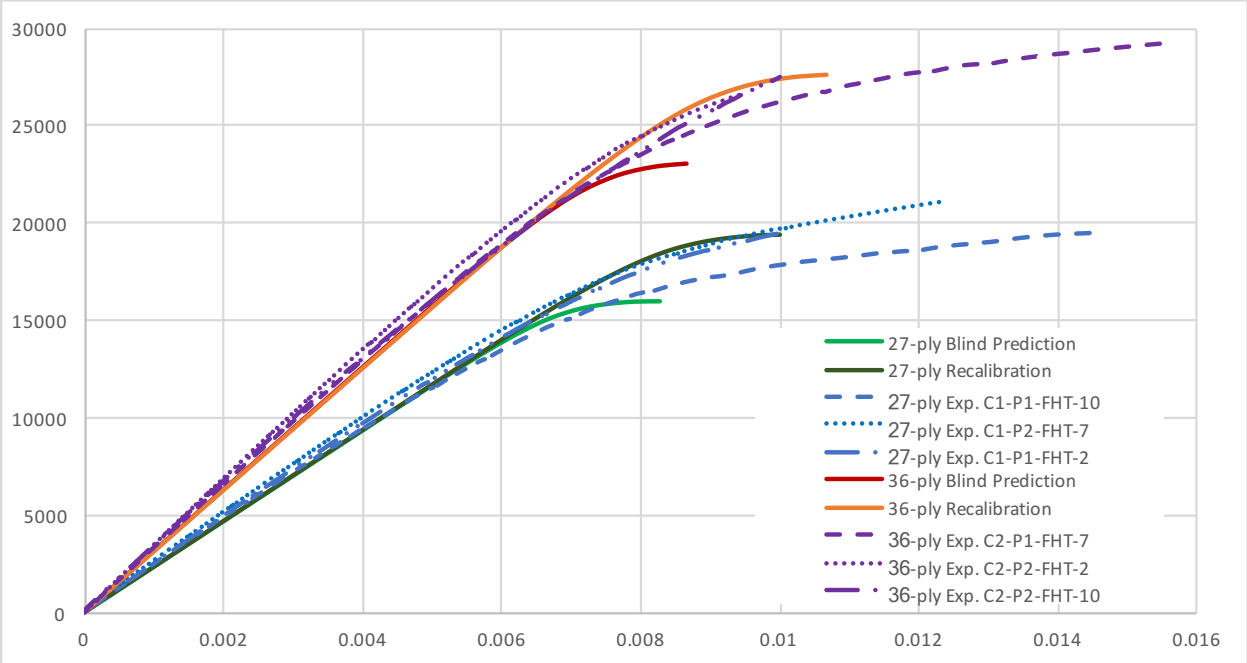

Figure 28. Static Open Hole tension P-d curve recalibration

5.3 Filled Hole Model Static Predictions

The FH static tests were a logical next step experiment to the OH predictions, introducing the complications of contact and preloading on the bolt. This case demonstrated the model's ability to predict the bypass portion of load transfer in a bolted joint situation, as no load is carried by the bolt but rather all of the load is carried through the specimen around the bolt.

5.3.1 Blind Predictions

Stress and strain were calculated in the same way as in the OH cases. The force displacement curves are shown in Figure 29, as compared with the experimental data curves and OH predictions.

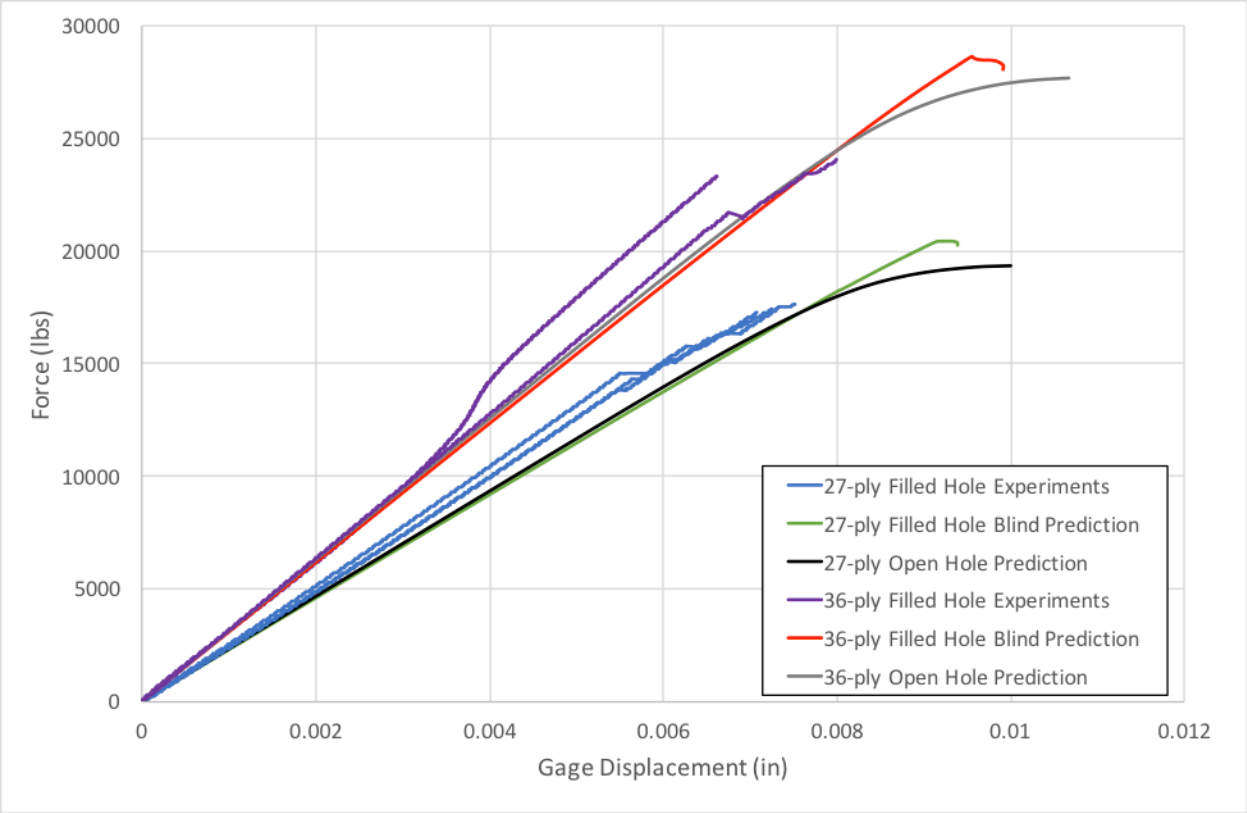

Figure 29. Static Filled Hole tension P-d curve blind prediction, including Open Hole prediction for comparison

Both configurations show excellent stiffness match, but significant over prediction of strength. This error is especially noteworthy in that it changes the comparison of behavior between the OH and FH cases. The experiments show that the FH cases should fail before the OH cases, whereas in our predictions, this phenomenon is reversed. There is some discrepancy in the literature as to whether an FH specimen should predict a higher residual strength than a corresponding OH specimen experiment. Yan et. al. [21] found that for graphite reinforced epoxy, in specimens with a high percentage of 0 degree plies, the OH strength exceeds the FH tension strength. The damage patterns for those same specimens show clear difference not seen in the Project 2 experimental results. It is possible that the behavior in that case could be attributed not to the high percentage of 0 degree plies, but the fact that every specimen in that group had thick 0 plies. A different experimental investigation performed on CFRP layups very similar to the current layups showed a failure load for FH tension cases on average about 3% higher than in the OH tension experiments [22]. Gamdani et. al. [23] noted that the body of experimental literature does not agree on

whether filling OH experiments increases or decreases their ultimate strength capacity; furthermore, the experiments they performed as part of their study supported the findings that FH experiments resulted in a lower ultimate strength, though for the carbon fiber specimens, the difference between the two cases was only about 3%.

The final predicted damage state (i.e., damage state at the peak of the P-d curve) of fiber damage, matrix damage, and delamination damage on the specimens are shown in Figure 30 for Configuration 1 and in Figure 31 for Configuration 2.

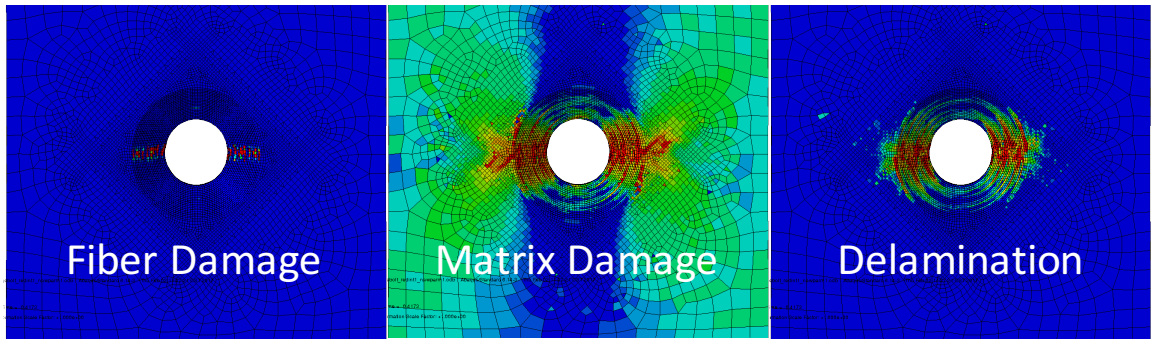

Figure 30. 27-ply (Configuration 1) Filled Hole damage pattern predictions for fiber, matrix, and delamination damage

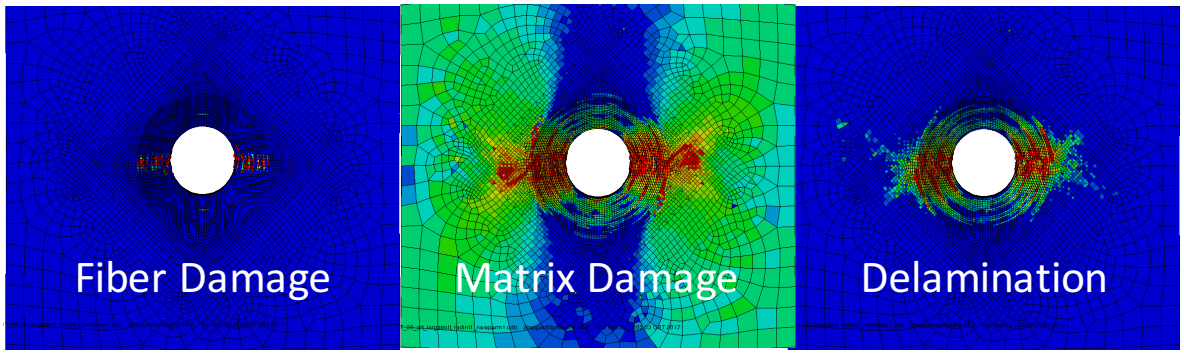

Figure 31. 36-ply (Configuration 1) Filled Hole damage pattern predictions for fiber, matrix, and delamination damage

For qualitative comparison, a representative picture of the damage state from the FH experiments is shown in Figure 32.

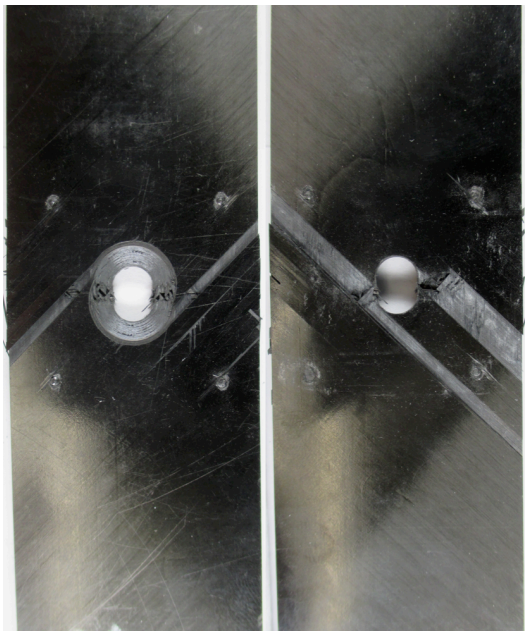

Figure 32. Filled Hole experimental overall damage patterns for qualitative comparison

From this comparison, two observations are made. First, the overall damage patterns seem to match the simulation results quite well. Second, as shown in the predicted damage states, the pattern of damage as compared between the OH and FH simulations is very similar, but the cracks in the FH cause do not spread as far as those in OH at the points of respective failure. This implies that the reason the FH tests show less ultimate strength than their OH counterparts has to do with the confining effect of bolt preload rather than a more severe onset of damage because of the presence of the bolt in the system.

5.3.2 Recalibration

In Abaqus modeling, to ensure proper contact modeling, the slave surface in the contact pair ought to have a smaller mesh density than the master surface. In the case of the contact between the specimen and bolt, in our model, the specimen must be the master surface and the bolt the slave surface. In the recalibration phase, the use of a smaller, more accurate bolt mesh was investigated. The larger bolt mesh used seed size of 0.01 inches, and the smaller bolt mesh used seed size of 0.0053 inches (the specimen ply and element thickness). In this investigation, it was determined that including some contact stabilization would resolve the numerical convergence issues associated with the more accurate contact representation, provided a large enough stabilization factor. If requested, Abaqus automatically calculates a

value for contact stabilization applied, but the user can adjust the value by a specified factor. A parametric study was performed to determine the level of contact stabilization that would capture a peaking of the load-displacement curve, while not introducing spurious strength. Figure 33 shows the effect of different values of the contact stabilization factor on the load-displacement curve for the 27-ply FH specimen under the same static tension test.

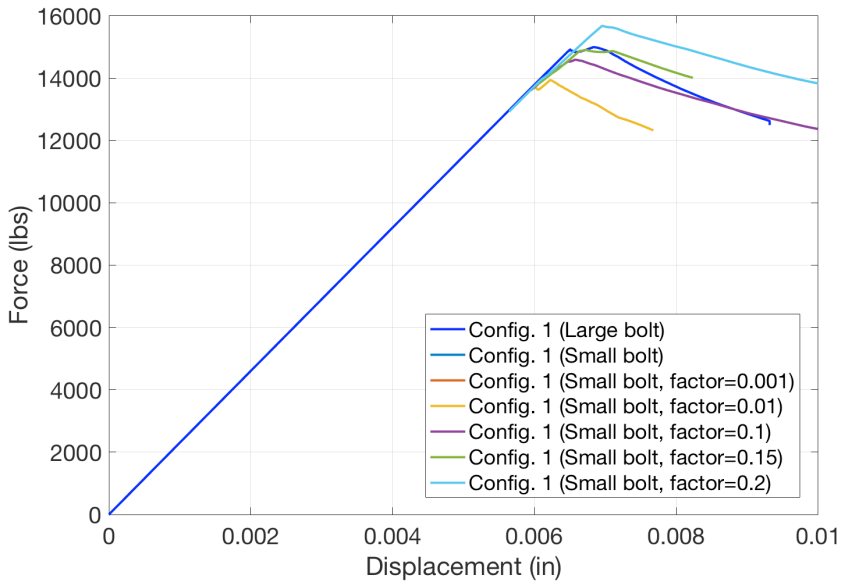

Figure 33. Comparison of using small bolt mesh with various contact stabilization factors compared with using large bolt mesh, using old material parameters

From this parametric study, it can be seen that the results are extremely sensitive to the value used for the stabilization factor and that the stabilization factor must significantly knock down the value Abaqus would automatically use. Additionally, using the smaller bolt mesh with contact stabilization significantly reduces the value of the ultimate strength. For the case in the parametric study, it was shown that the smallest value for contact stabilization that would also allow enough convergence to show a peak in the force displacement curve was 0.01. Though the FH blind predictions were performed with the recalibrated material properties from the OH simulations, this parametric study was performed using the older set of material properties. When the newer properties were used, contact stabilization of 0.01 was not enough to show a peak in the curve; thus, the contact stabilization was increased to 0.02 for the recalibrations. A limited comparison of the contact stabilization factors using the recalibrated material properties is shown in Figure 34, proving that 0.02 is the smallest

stabilization factor to allow for convergence while showing a clear peak for these simulation cases.

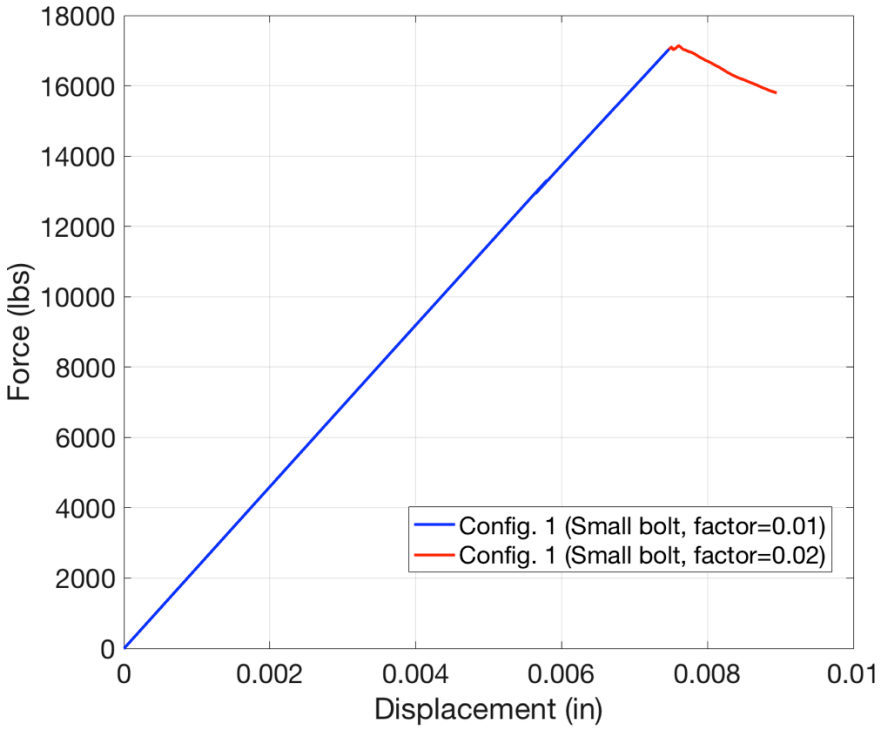

Figure 34. Comparison of using small bolt mesh with stabilization factors, using current material parameters

Thus, the small bolt mesh with contact stabilization of 0.02 was used for the FH tension recalibration simulations. The recalibrated results compared with experimental data and the blind predictions are shown in Figure 35 and display good agreement both in stiffness and ultimate strength prediction.

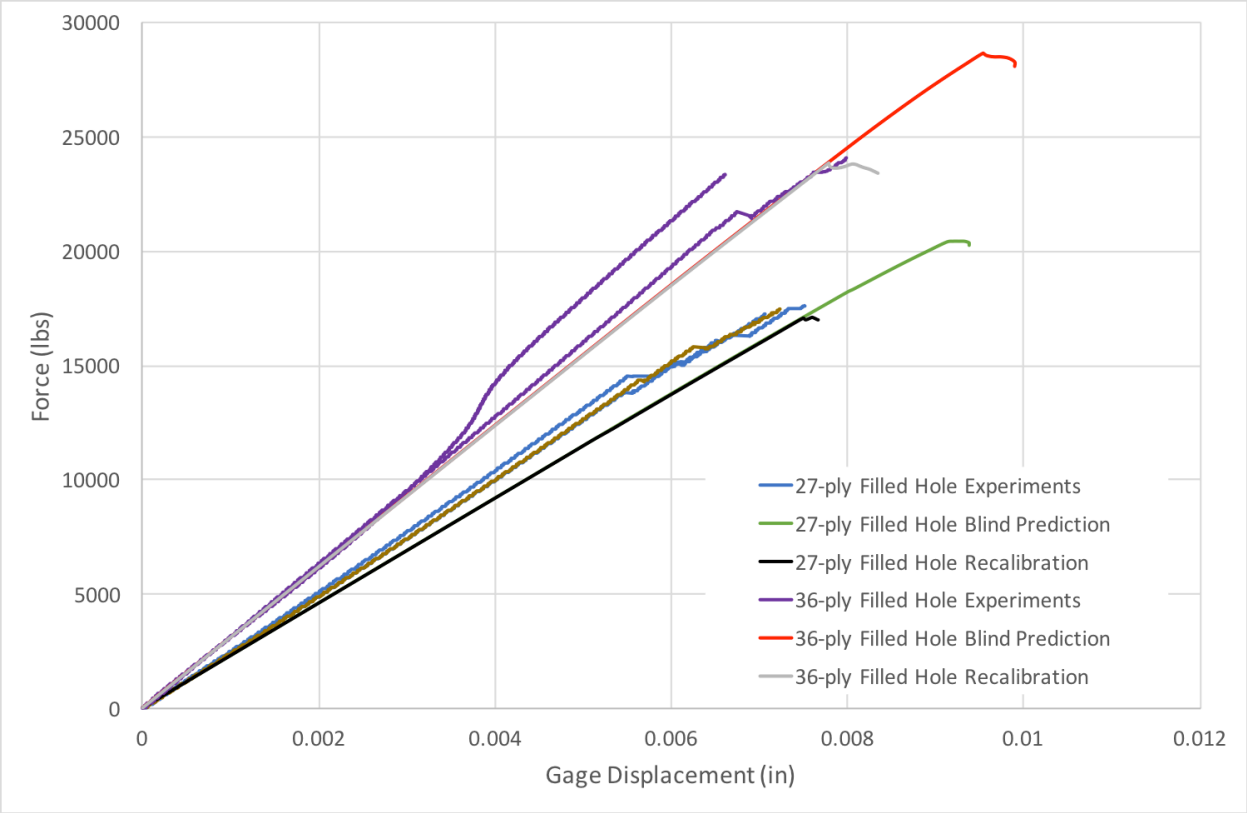

Figure 35. Static Filled Hole tension P-d curve recalibration

Because this recalibration only pertained to the bolt mesh and contact properties, it does not affect the previous results from the OH cases.

5.4 Single Shear Bearing Model Static Predictions

As the FH tests were intended to replicate a pure bypass type behavior, the single shear bearing tests replicated a pure bearing behavior, where all of the load is transferred through the bolt to the fixture. This case introduces further complexity, similar to the Stage 1 IRAD configuration simulations, in that there is contact between both the bolt and the specimen, but also between the bolt and the fixture and the specimen and the fixture. The SSB predictions can verify the model's ability to establish the correct stiffness in a bearing case, further corroborating the results from the OH and FH tests that the model can capture the correct stiffness when bearing is not involved. Additionally, this provided another test case with which to develop the model to better predict post-peak failure under bearing loading conditions.

Force was defined as the sum of reaction forces on the pulled face, and displacement was calculated by a virtual crack opening displacement (COD) gage held between one brace attached to the fixture and a knife edge brace attached to the specimen; the original displacement between the reference points was 1 inch, as shown in Figure 36.

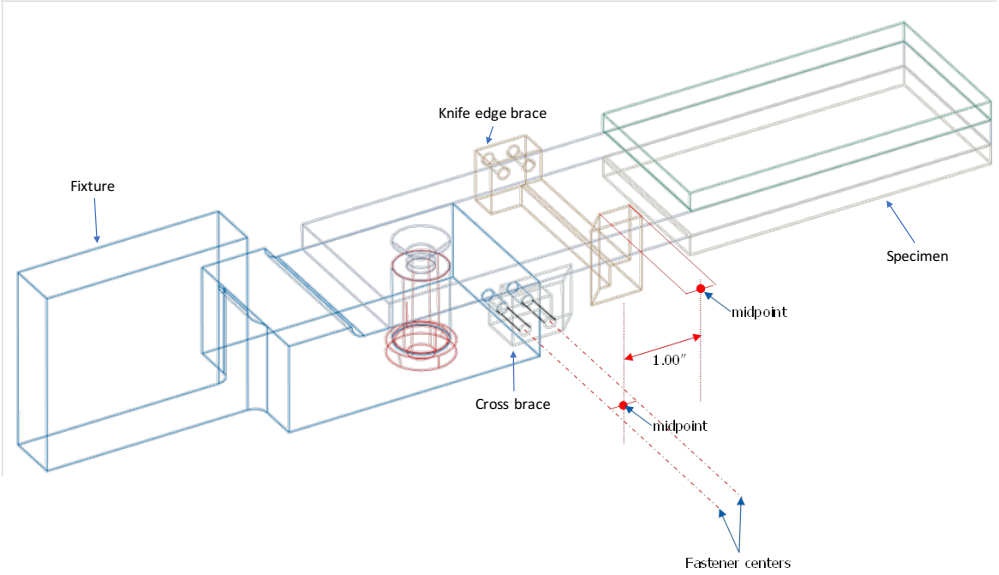

Figure 36. Single Shear Bearing strain measurement setup for COD gage (figure used courtesy of Jonathan Bartley-Cho of Northrop Grumman Corporation)

5.4.1 Modeling Method Developments

Before the blind prediction simulations, a variety of developments in modeling methods were investigated.

5.4.1.1 Elastic Tests for Convergence Issues

In order to determine the extent of numerical convergence problems related to contact, a series of tests were performed with the 27-ply version of the SSB tests, where the specimen was modeled as an elastic material rather than a damageable material (all other parts of the modeling were left the same). A prediction of this sort resulted in Figure 37.

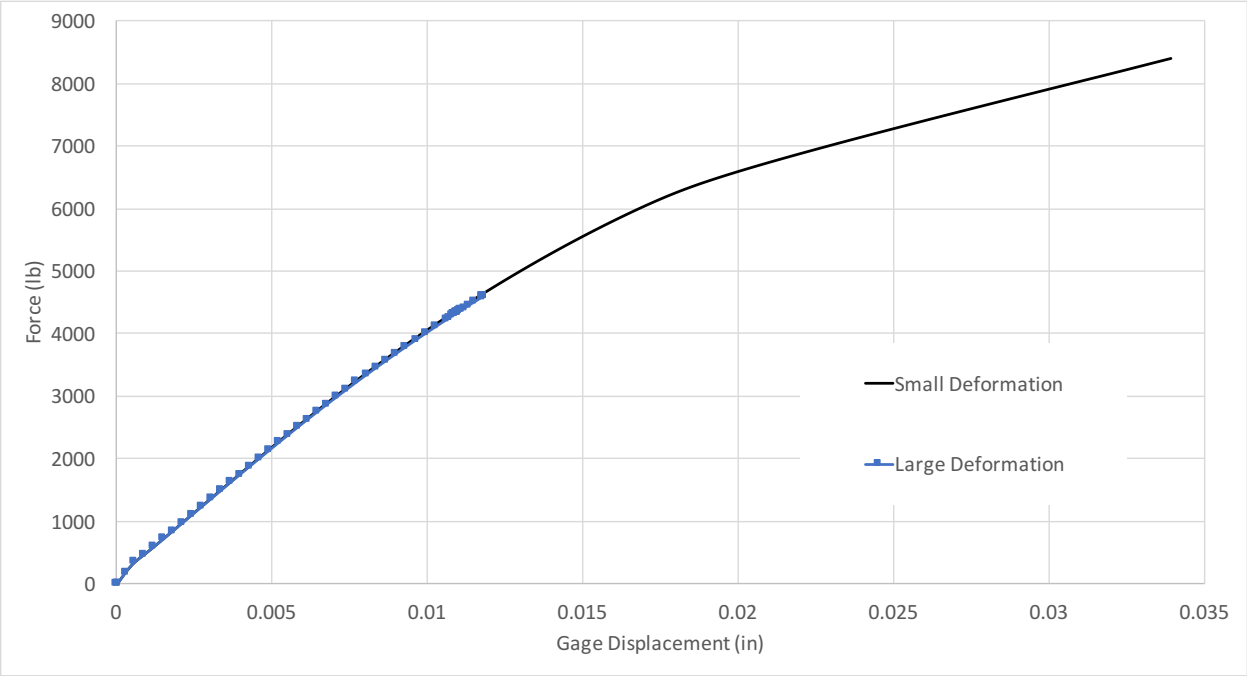

Figure 37. 27-ply (Configuration 1) Single Shear Bearing elastic specimen, plastic bolt test, using large and small deformation formulations

While this elastic test did indeed converge, the bolt behavior seen in the IRAD experiments and through initial SSB model testing was significant enough to no longer be able to be considered as small deformation. Therefore, a large deformation formulation needed to be considered. The large deformation elastic specimen simulation failed to converge about one third of the way through the loading cycle, also shown in Figure 37. Because the specimen in this case was not damageable, all convergence issues emanated from contact and the presence of large strain iterations.

5.4.1.1.1. Options for Contact Type

Abaqus can define contact through one of two different methods. There are minor differences between these two methods, but the significant differences lie in the way they are defined and in the default contact tracking approaches. The first is called general contact, and it requires no explicit definition of which surfaces may be in contact; it then finds the surfaces which touch during the simulation and applies contact between those surfaces. The second is called contact pairs, which requires identifying which surfaces should have contact

defined between them. If contact is between two distinct surfaces, by specifying specific types of contact with specific tracking approaches, the differences between the two methods fade; so, for the purposes of this study, the contact pair method was used.

Using either of the methods, contact is defined by one of two types and one of two tracking approaches. The type can either be surface to surface contact or node to surface contact. Surface to surface contact considers the shape of the contact surfaces while node to surface interpolates the values of the master nodes nearest to the slave node's projection on the master surface. The user can also define how contact is tracked throughout the simulation. Finite sliding type tracking, though potentially computationally costly, allows any arbitrary movement between the contact surfaces. Small sliding, on the other hand, assumes that even if the bodies undergo large deformation, they experience it together; that is, regardless of the overall behavior, there is relatively little sliding (on the order of a fraction of the element length) of one surface against the other. In view of significant overturning of the bolt in elastic SSB simulations, the finite sliding formulation with surface to surface type contact is employed. The results of the elastic specimen simulation using finite sliding as opposed to small sliding is shown in Figure 38. Two conclusions can be drawn from these simulations. First, using the large deformation solution formulation significantly alters the overall P-d curve prediction for this case. Second, the finite sliding contact formulation should be used both from a physical behavior justification and from a convergence perspective.

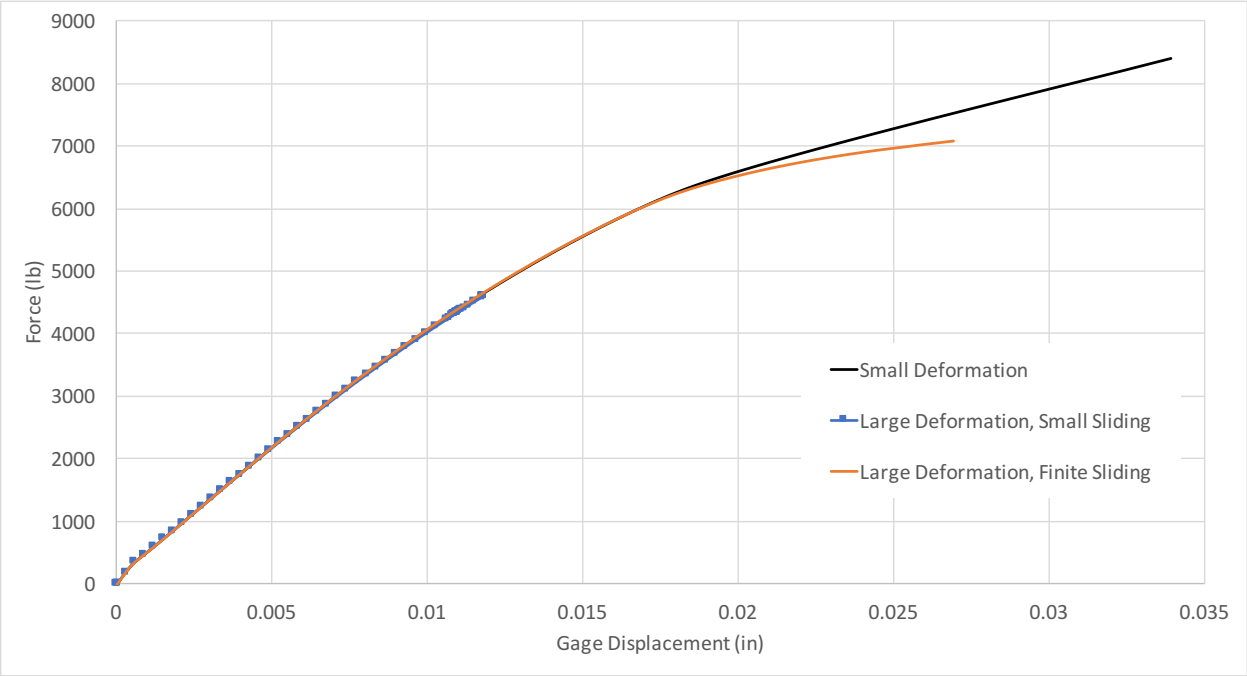

Figure 38. 27-ply (Configuration 1) Single Shear Bearing elastic specimen, plastic bolt test, using small and finite sliding contact approaches

5.4.1.1.2. Fixture and Specimen Representation

In this study of the SSB configurations, two different geometric representations were considered for the fixture. The first representation considered rested on the assumptions employed on the SLEP-C and IRAD fixtures, which were that the bolt and fixture essentially move together and could thus be considered a single body, tied together. In the second representation, the bolt was considered as a separate piece in contact with the rest of the fixture instead of using tie constraints; this would allow the bolt to bend more freely due to the specimen bearing against it. Using the second type of fixture representation showed a significantly lower value for stiffness than with using the method employed with the SLEP-C and IRAD simulations, as shown in Figure 39. After observing the impact these assumptions had on the stiffness of the system, one additional fixture representation was considered. Between the bolt and the fixture in the experiments, a bushing was used as an exchangeable buffer to keep the fixture from damaging. The third fixture representation modeled the bolt, bushing, and fixture all as separate entities, simply in contact with each other. This

representation showed very little stiffness difference from the case where only the bolt was separated, which means that it can be safely assumed the bushing and fixture act as one piece and can be modeled as such.

Furthermore, in order to improve the convergence of these simulations, the specimen was remeshed as a single part, rather than as separate plies, with a regularized, non-fiber-aligned mesh. This mesh in a damage simulation may introduce some additional error in capturing the direction of damage progression.

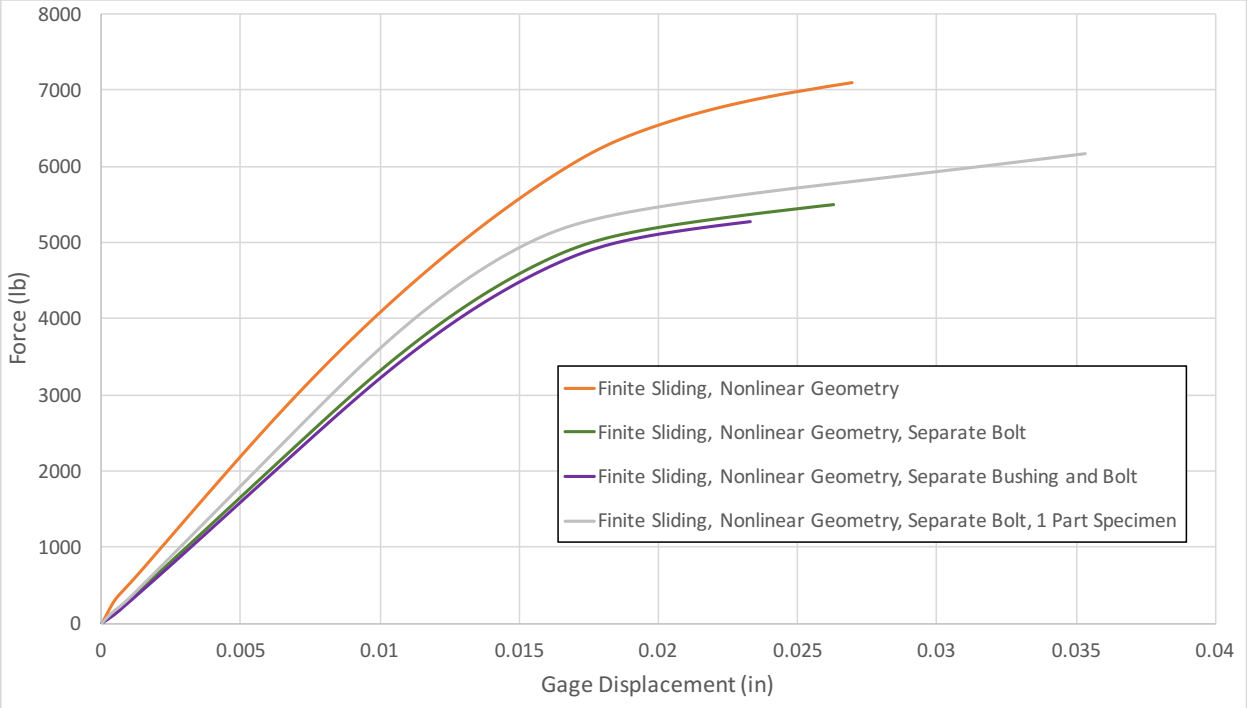

Figure 39. 27-ply (Configuration 1) Single Shear Bearing elastic specimen, plastic bolt test, with various geometric representations

5.4.2 Blind Predictions

Using the findings from the modeling method developments, blind predictions were performed using the same residual stiffness idea, enforced at 94% of damage, used for the IRAD and SLEP-C configurations. Following the conclusions from previous test simulations, the bolt was modeled as distinct from the fixture with a small mesh (congruent with the FH tests), the specimen was modeled as one part without ply fiber-aligned meshes, a contact stabilization factor of 0.02 was applied, and the finite sliding contact formulation was

enforced in conjunction with the large deformation capability to capture the significant overturning behavior observed even in the elastic specimen simulations.

The force displacement curves extracted from the simulation results are given in Figure 40 through Figure 43 for Configuration 1 tension test, Configuration 2 tension test, Configuration 2 compression test, and Configuration 3 tension test, respectively. The predictions for both Configuration 2 tests failed to converge beyond the curves shown, even though the same exact same modeling methods were employed as those which provided convergence for Configurations 1 and 3.

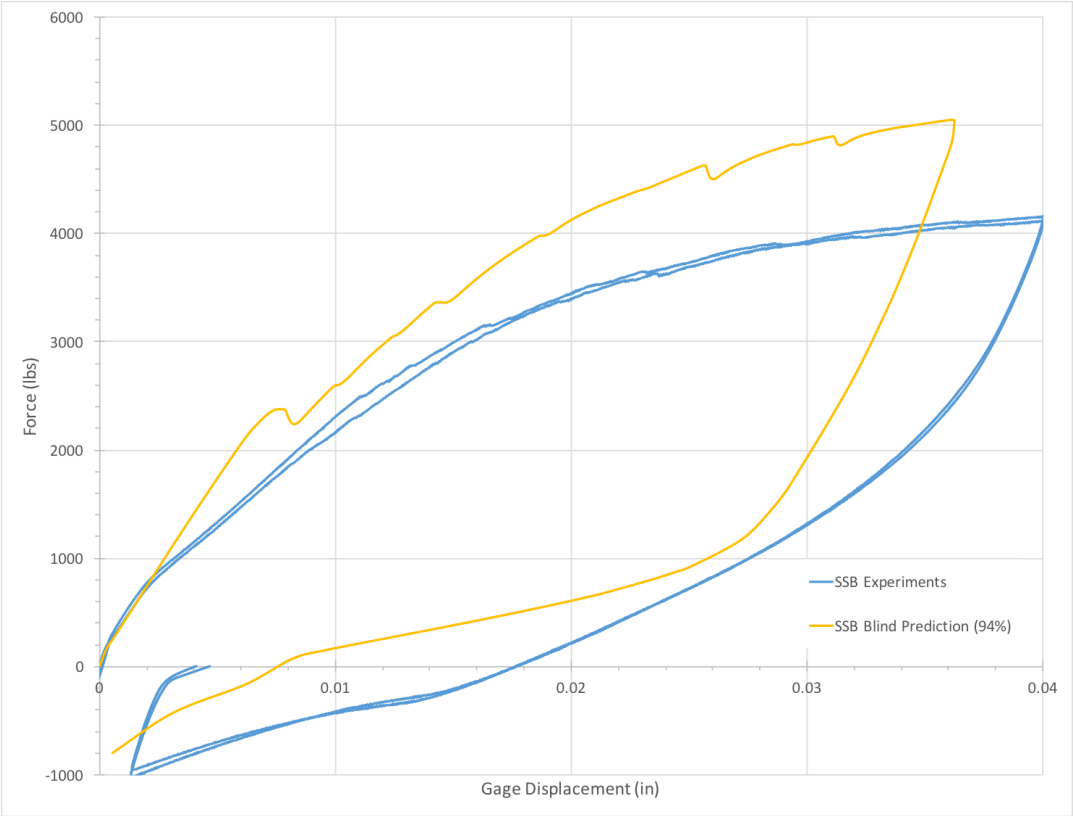

Figure 40. 27-ply (Configuration 1) Single Shear Bearing tension P-d curve blind prediction

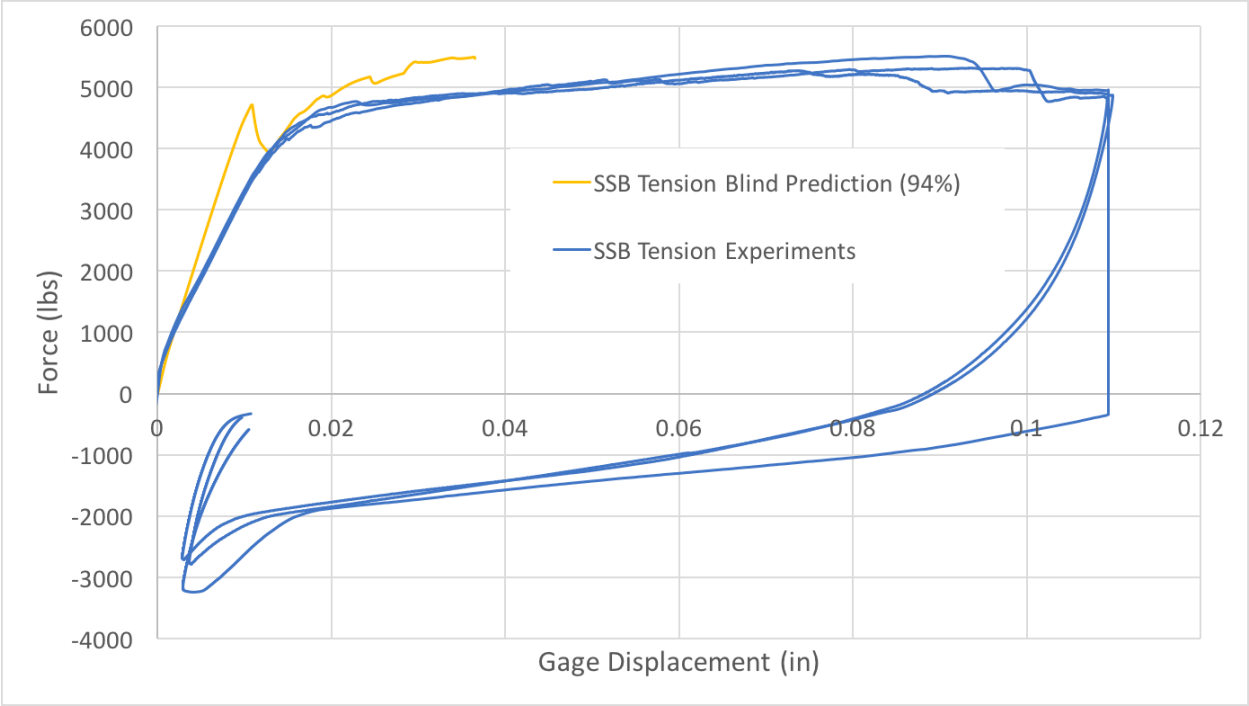

Figure 41. 36-ply (Configuration 2) Single Shear Bearing tension P-d curve blind prediction

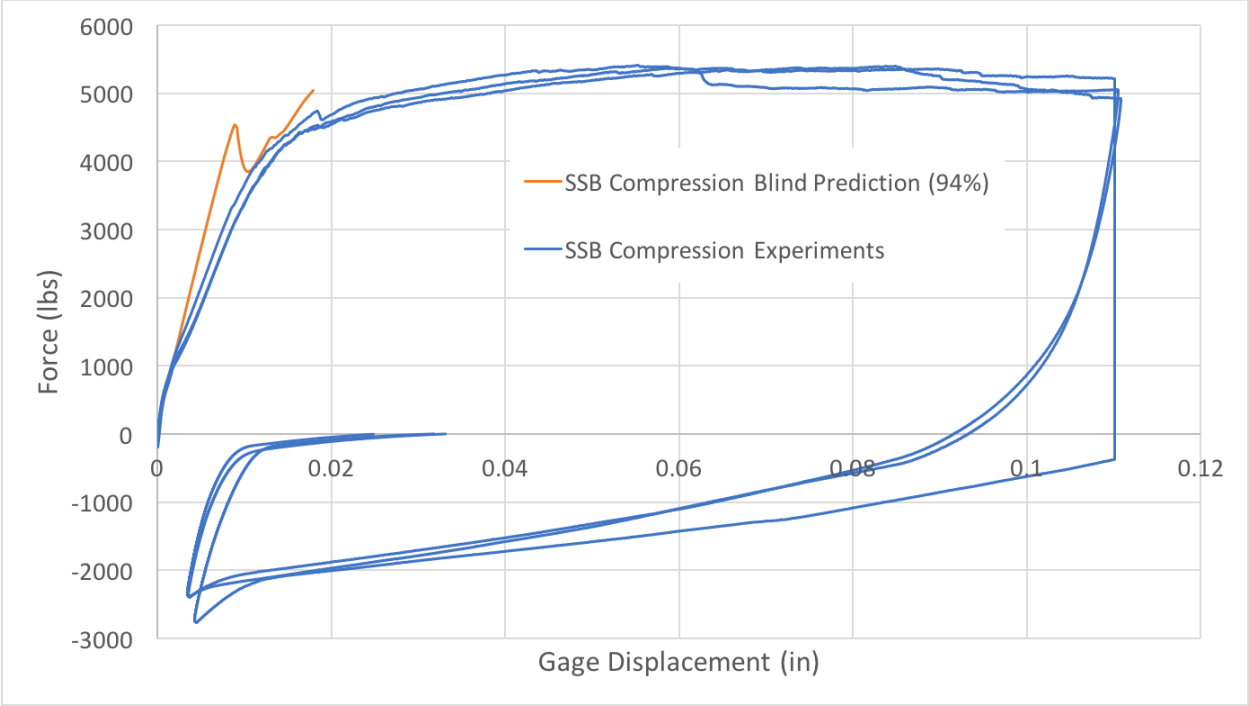

Figure 42. 36-ply (Configuration 2) Single Shear Bearing compression P-d curve blind prediction

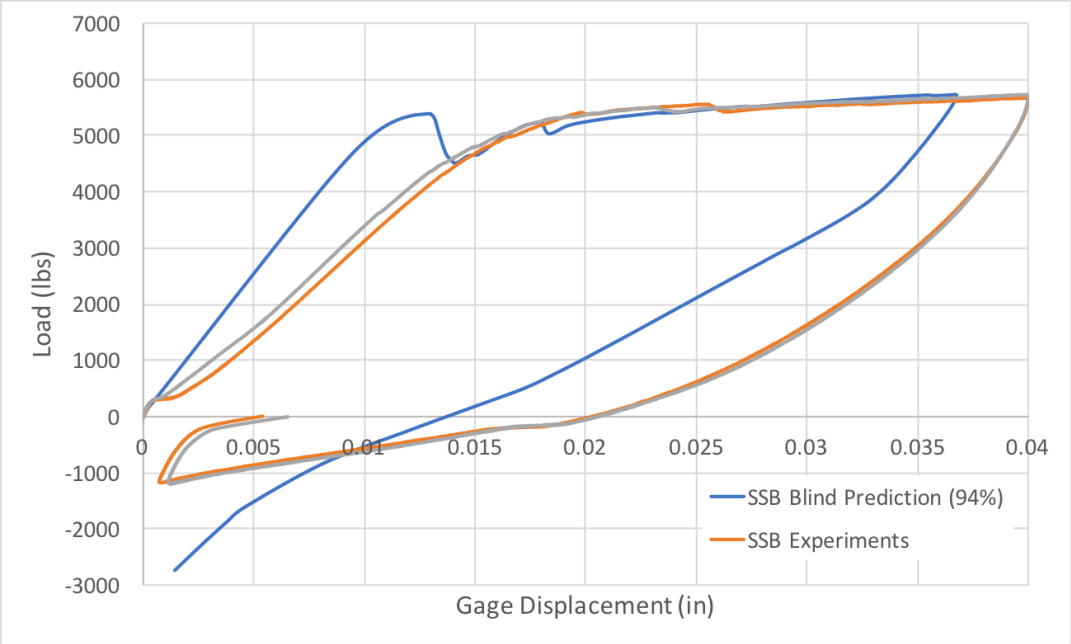

Figure 43. 45-ply (Configuration 3) Single Shear Bearing tension P-d curve blind prediction

Under these conditions, the plasticity of the bolt plays an important role in the overall behavior, and is, as the composite material model stands, the sole contributor to the permanent deformation shown in the unloaded P-d curves. The deformation of the bolt at peak loading and at the full unloaded position from the Configuration 1 SSB tension test, as representative of the bolt behavior in all the SSB cases, is given in Figure 44.

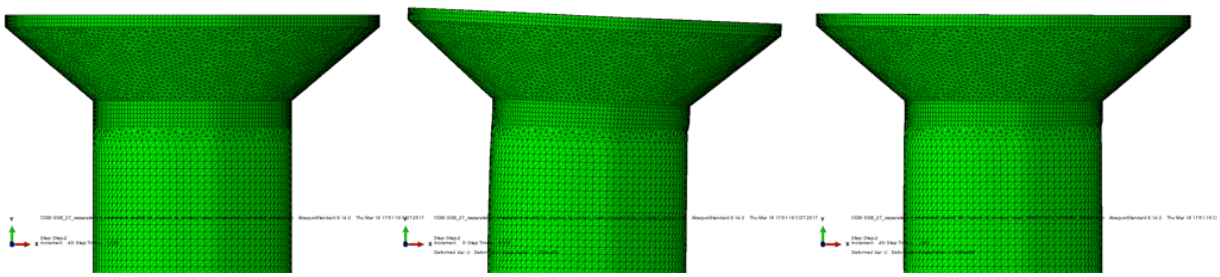

Figure 44. Bolt Deformation at pristine, peak load, and full unload from 27-ply (Configuration 1) tension Single Shear Bearing test

5.4.3 Recalibration Studies

From the blind prediction results, it was clear that while the preliminary stiffness issue seems to have been addressed in allowing the bolt to move freely from the fixture, there is

still an issue in prediction once the first nonlinearity appears in the experimental curves, of growing influence with the thicker specimens. Additionally, the bolt post-peak behavior still requires additional development. Though the residual stiffness method added too much stiffness to the specimen after damage, the overall behavior seemed to be captured reasonably well. A few simulations were performed to investigate further the role of the value for the damage percentage at which the residual stiffness was imparted in these SSB simulations. Using residual stiffness at 97% damage quickly proved to also confer too much stiffness, at which point the analysis was aborted. Results for using residual stiffness at 99% damage with the 27-ply SSB test are given in Figure 45; the simulation failed to converge at about 60% of the loading cycle, but the post-peak behavior up unto this point shows excellent match with the experiments.

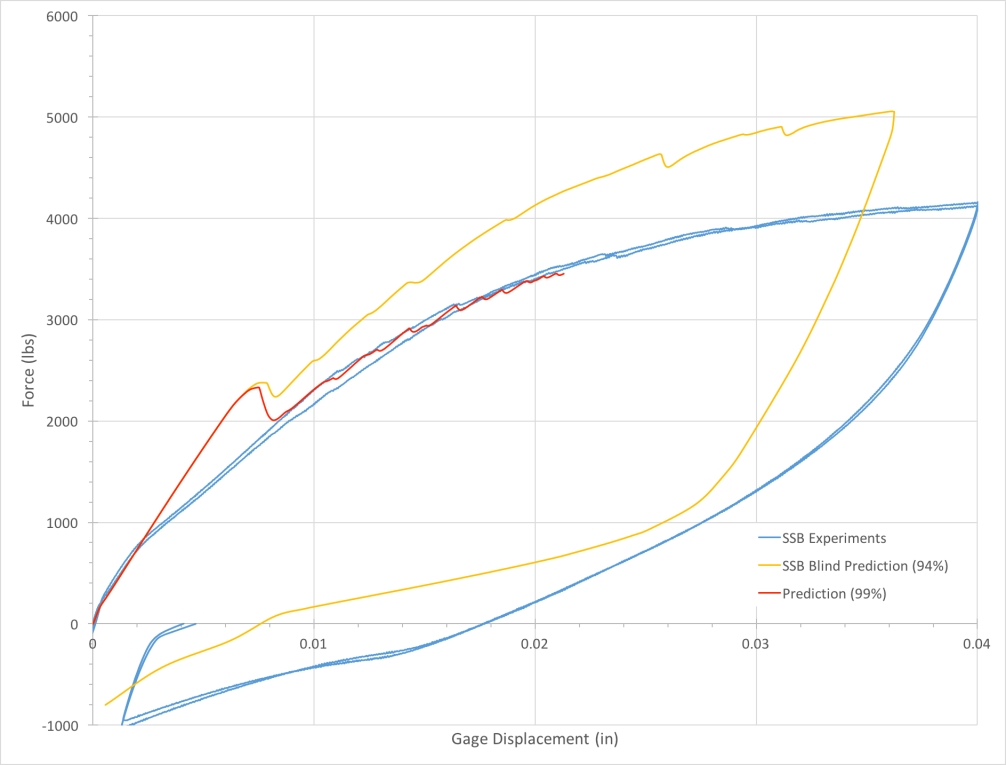

Figure 45. 27-ply (Configuration 1) Single Shear Bearing tension P-d curve recalibration using residual stiffness at 99% damage

CHAPTER 6

CONCLUSIONS AND FUTURE RESEARCH

Overall, the static predictions performed as part of this thesis work have shown EHM to be a robust material model, useful for the behavioral prediction of IM7/977-3 composite bolted joints. Though there is yet improvement required in ensuring the post-peak prediction capabilities, the current work shows that the stiffness of these experimental systems can be accurately captured and the residual stiffness method shows good promise in capturing the post-peak behavior. Over the course of this project, modeling methods have been refined to capture the physical behavior of the systems; contact between the bolt and specimen must be allowed to move significantly relative to each other, the bolt must be allowed to overturn and not necessarily be constrained by the movement of the fixture, and a variety of tools to help with convergence issues have been tested for implementation when necessary. The model shows great promise to be able to be used for damage prediction. The OH and FH test predicted damage patterns match the experimental results very well; in this case, the model was able to show that though the damage patterns between the two cases showed very little difference, the presence of the bolt caused an early onset of failure for the FH test, just like the experiments. Furthermore, the overall force-displacement behavior is extremely well captured by the EHM predictions as compared to the experiments for both OH and FH tests with both configurations used. While further investigation and development is yet to be performed on bearing-type configuration cases, the EHM force displacement predictions are reasonable, and by studying further the residual stiffness damage percentage parameter, these results show promise that EHM is a reliable choice for composite bolted joint damage analysis. With the capability of capturing the mechanical response of composite bolted joints, the flexibility of EHM has been dramatically increased, making it an ever more attractive choice for the tool aerospace vehicle computational modeling needs.

A significant amount of research and development work remains on composite bolted joints. The bearing bypass mechanism has not yet been explored in EHM modeling; static predictions of this sort would yield important information necessary for reliable prediction of the multi-bolt joint simulations. Recalibration studies on the SSB experimental configurations are

necessary to ensure that the modeling approach is further progressed to robustly capture the desired results. These tests may include further residual stiffness and residual strength development activities, modifying the material behavior under shear, or another type of recalibration.

Furthermore, to ensure that EHM can assess the damage tolerance of these advanced composite materials, the fatigue behavior of the composite joints must be studied. While accurate static predictions are crucial to obtaining the correct results under fatigue, fatigue loading may introduce material behavior not yet observed under static loading. While EHM is computationally efficient compared to its counterparts, these simulations with hundreds of thousands of elements are very costly, so to be able to run many loading and unloading cycles in fatigue, further research is necessary on computational efficiency measures, whether through the mathematical formulation or through model reduction schemes.

Future model investigations could also include researching methods to reduce mesh bias to simplify the modeling process, which would have particular benefit if this model were to be used in complicated shapes of real structural components. Because the mesh affects the specimen response, a standard procedure should be developed that is specific but also flexible for a variety of specimens or structural components. Additionally, the version of EHM currently being developed for more controllability in the material softening behavior and for mesh size insensitivity could be used to simplify the meshing process. Since contact causes such trouble with convergence and complexity in modeling, methods of simplifying this contact modeling could also prove to be a worthwhile endeavor.

REFERENCES

[1] P. P. Camanho, S. Bowron, and F. L. Matthews, “Failure Mechanisms in Bolted CFRP,” *Journal of Reinforced Plastics and Composites*, 17:205-233, 1998.

[2] H.-S. Wang, C.-L. Hung, and F.-K. Chang, “Bearing Failure of Bolted Composite Joints. Part I: Experimental Characterization,” *Journal of Composite Materials*, 30:1284-1313, 1996.

[3] I. Eriksson, “On the bearing strength of bolted graphite/epoxy laminates,” *Journal of Composite Materials*, 24:1264-1269, 1990.

[4] R. A. Naik and J. H. Crews, Jr., “Ply-Level Failure Analysis of a Graphite/Epoxy Laminate Under Bearing-Bypass Loading,” Composite Materials: Testing and Design (Ninth Volume), ASTM STP 1059, S. P. Garbo. Ed., American Society for Testing and Materials, Philadelphia, 191-211, 1990.

[5] C. Oskay and J. Fish, "Eigendeformation-based Reduced Order Homogenization for Failure Analysis of Heterogeneous Materials," *Computer Methods in Applied Mechanics and Engineering*, 196(7):1216-1243, 2007.

[6] R. Crouch and C. Oskay, "Symmetric Meso-Mechanical Model for Failure Analysis of Heterogeneous Materials," *International Journal for Multiscale Computational Engineering*, 8:447-461, 2010.

[7] P. A. Sparks and C. Oskay, “The Method of Failure Paths for Reduced-Order Computational Homogenization,” *International Journal for Multiscale Computational Engineering*, 14:515-534, 2016.

[8] J. M. Guedes and N. Kikuchi, “Preprocessing and postprocessing for materials based on the homogenization method with adaptive finite element methods.,” *Computer Methods in Applied Mechanics and Engineering*, 83: 143–198, 1990.

[9] R. D. Crouch, S. B. Clay and C. Oskay, “Experimental and Computational Investigation of Progressive Damage Accumulation in CFRP Composites,” *Composites Part B*, 48:59-67, 2013.

[10] M. Bogdanor and C. Oskay, "Prediction of Progressive Damage and Strength of IM7/977-3 Composites using the Eigendeformation based homogenization approach: Static Loading.," *Journal of Composite Materials*, in press, 2016.

[11] R. Crouch, C. Oskay and S. Clay, "Multiple Spatio-Temporal Scale Modeling of Composites Subjected to Cyclic Loading," *Computational Mechanics*, 51:93-107, 2013.

[12] R. D. Crouch and C. Oskay, "Accelerated Time Integrator for Multiple Time Scale Homogenization," *International Journal for Numerical Methods in Engineering*, 101:1019-1042, 2015.

[13] M. J. Bogdanor and C. Oskay, "Prediction of Progressive Fatigue Damage and Failure Behavior of IM7/977-3 Composites using the Reduced-Order Multiple Space-Time Homogenization Approach," *Journal of Composite Materials*, in press, 2016.

[14] C. Oskay and J. Fish, "A multiscale model of composite failure under impact," *Proceedings of the ASME International Mechanical Engineering Congress and Exposition,* Chicago, IL, November 5-10, 2006.

[15] H. Yan, C. Oskay, A. Krishnan and L. R. Xu, "Compression After Impact Response of Woven Fiber Reinforced Composite," *Composites Science and Technology*, 70:2128-2136, 2010.

[16] A. Krishnan and C. Oskay, "Modeling Compression-After-Impact Response of Polymer Matrix Composites Subjected to Seawater Aging," *Journal of Composite Materials*, 46:2851-2861, 2012.

[17] T. Hui and C. Oskay, "Computational Modeling of Polyurea-Coated Composites Subjected to Blast Loads," *Journal of Composite Materials*, 46:2167-2178, 2012.

[18] M. J. Bogdanor, S. Mahadevan and C. Oskay, "Uncertainty Quantification in Damage Modeling of Heterogeneous Materials," *International Journal for Multiscale Computational Engineering*, 11:289-307, 2013.

[19] M. J. Bogdanor, C. Oskay and S. B. Clay, "Multiscale Modeling of Failure in Composites under Model Parameter Uncertainty," *Computational Mechanics*, 56:389-404, 2015.

[20] M. J. Bogdanor, "Failure Prediction of Fiber Reinforced Composites Using Reduced Order Multiscale Models," Ph.D. dissertation, Department of Civil & Environmental Engineering, Vanderbilt University, Nashville, TN, 2015.

[21] Y. Yan, W.-D. Wen, F.-K. Chang, and P. Shyprykevich, "Experimental study on clamping effects on the tensile strength of composite plates with a bolt-filled hole," *Composites: Part A*, 30:1215-1229, 1999.

[22] J. Zhang, F. Liu, L. Zhao and M. Shan, "Investigation on characteristic length testing methods for failure prediction of composite multi-bolt joints", *Journal of Reinforced Plastics and Composites*, 34(8):636-648, 2015.

[23] F. Gamdani, R. Boukhili and A. Vadean, "Tensile strength of open-hole, pin-loaded and multi-bolted single-lap joints in woven composite plates", *Materials & Design*, 88:702-712, 2015.